Aerosol Jet Printed plasma actuators: Optical and electromechanical characteristics

Konstantinos Kourtzanidis, M. Karani, N. Vlachos, P. Dimitrakellis, D. Tsekourakis, N. Hastas, V. Pattanshetti, Marios Kotsonis, N. Fagnon, Dimitrios Stefas, et al.

Sensors & Actuators: A. Physical 403 (2026) 117702

Contents lists available at ScienceDirect

Sensors and Actuators: A. Physical

journal homepage: www.journals.elsevier.com/sensors-and-actuators-a-physical

Aerosol Jet Printed plasma actuators: Optical and electromechanical characteristics

K. Kourtzanidis [a,*], M. Karani [a], N. Vlachos [a], P. Dimitrakellis [a], D. Tsekourakis [a], N. Hastas [b], V. Pattanshetti [c], M. Kotsonis [c], N. Fagnon [d], D. Stefas [d], K. Gazeli [d]

[a] Advanced Renewable Technologies for Energy & Materials Integrated Systems (ARTEMIS) Laboratory, Chemical Process & Energy Resources Institute (CPERI), Centre for Research & Technology, Hellas (CERTH), Thessaloniki, Greece
[b] Sector of Condensed Matter and Material Physics, School of Physics, Aristotle University of Thessaloniki (AUTH), Thessaloniki, Greece
[c] Department of Flow Physics and Technology, Delft University of Technology, Delft, the Netherlands
[d] Laboratoire des Sciences des Procédés et des Matériaux (LSPM), CNRS, Université Sorbonne Paris Nord, UPR 3407, Villetaneuse F—93430, France

ARTICLE INFO

Keywords:
Plasma actuators
Aerosol jet printing
Dielectric barrier discharge
Electrohydrodynamic flow
Ionic wind
Flow control

ABSTRACT

We present a novel promising fabrication technique for Surface Dielectric Barrier Discharge (SDBD) plasma actuators based on Aerosol Jet Printing (AJP) technology of conductive inks on dielectric surfaces and characterize the AJP-SDBDs optical and electromechanical performance. Linear SDBD designs, with ultra-smooth electrode edges of micrometer thickness have been fabricated, which when driven by AC, High Voltage waveforms, present stable plasma operation and reproducible features. We measure the electromechanical characteristics in terms of ink-related electrical properties (through Van der Pauw-resistivity and Hall measurements), plasma properties through electrical diagnostics, time-resolved imaging and optical emission spectroscopy (OES), while we perform Particle Tracking Velocimetry (PTV) measurements of the induced wall-jet flow. The printed electrodes show a clear metallic behavior, with their electronic properties comparing very favorably to other printable materials. The AJP-SDBDs show similar electromechanical characteristics with conventional SDBDs fabricated via conventional methods, good robustness, and more intense nature indicating lower breakdown voltage requirements. The emission spectra from the discharge show dominant formation of excited N_2 and N_2^+ species. Based on high-resolution OES, an estimation of rotational and vibrational temperatures of the $N_2(C)$ state is performed, showing the strong non-equilibrium nature of the discharges produced. This helps in maintaining the average gas temperature in the positive and negative AC voltage phase at low levels (below 350 K) indicating its minimal impact on the gas dynamics. In terms of induced flow and electrohydrodynamic (EHD) forcing, the AJP-SDBD resulted in wall-jet flows with a maximum velocity achieved of approximately 5 m/s and a wall-jet height of approximately 3 mm at 7 mm from the exposed electrode edge for the 30 kV 3 kHz case. At the same conditions, the EHD force reached more than 27.5 mN/m. The obtained values and trends are in good agreement with literature values of conventional AC driven SDBD actuators, showcasing AJP potential as a promising fabrication technique for robust and efficient plasma actuators and related applications.

1. Introduction

Surface Dielectric Barrier Discharges (SDBDs) [1], have gained significant attention in various fields due to their ability to produce relatively strong and localized ElectroHydroDynamic/ElectroAeroDynamic (EHD - EAD) flows and/or ultra-fast gas heating and pressure/shock wave formation [2] via energy deposition while promoting reactivity and transport mechanisms. The induced jet-like flows arising under Alternating Current (AC) excitation, often referred to as ionic wind, can help control aerodynamic phenomena [3,4], promote mixing for combustion applications [5], enable film cooling [6], while the reactivity occurring in SDBDs finds applications in several high-impact fields such as selective anti-cancer [7] and water treatment [8]. In parallel, when operated in nanosecond pulsed mode [9], SDBD actuators find applications (among others) in plasma-assisted combustion as stimulants of kinetics [10] as well as a super/hypersonic shock wave control method [11]. However, SDBDs are often limited by fabrication constraints, leading to decreased robustness, longevity, repeatability, and flexibility

* Corresponding author.
E-mail address: kourtzanidis@certh.gr (K. Kourtzanidis).

https://doi.org/10.1016/j.sna.2026.117702
Received 3 November 2025; Received in revised form 27 February 2026; Accepted 4 March 2026
Available online 7 March 2026

in design, hindering their electromechanical performance and applicability. Furthermore, most current fabrication techniques, mainly mechanical and hand-handled, can hardly structure electrodes with fine features and complex geometrical shapes, which could potentially improve the plasma characteristics and EHD flows. SDBDs consist of typically thin, conductive layers, placed on both sides of a dielectric substrate in an asymmetric configuration. One of these layers plays the role of an air-exposed electrode while the other one is insulated by being embedded inside the dielectric substrate or sandwiched between two dielectric layers. Focusing on EHD force-producing excitation and ignoring nanosecond-pulsed operation here, an Alternating Current (AC) High-Voltage (HV) waveform is applied on one of the two electrodes (the other electrode being typically grounded), producing a surface plasma on the dielectric which in turn generates an EHD force on the surrounding flow. The conductive layers can be thin metal sheets of various shapes, typically made of copper (Cu), tungsten (W), stainless steel, silver (Ag) and various Ag – metal combinations, while the dielectric substrate is typically made of Kapton, PMMA, quartz glass or aluminum oxide (Al_2O_3). In most studies, the fabrication of SDBDs entails the usage of conductive foil/tape (of different thickness) glued (usually with epoxy resin adhesive) on the dielectric surface. This, essentially manual, fabrication procedure hampers both the repeatability and the optimization of the SDBD modules, both in terms of electrode shape quality (uniformity, alignment, smoothness), as well as in terms of design flexibility. The structure (edge pattern) as well as imperfections on (mainly) the exposed electrode structure can alter the plasma characteristics significantly (even leading to catastrophic failure due to intensified discharges emanating from sharp points which can cause dielectric erosion and breakdown) and also modify the directionality and magnitude of the induced flow [12–15]. In addition, the thickness of the exposed electrode plays an important role on both the discharge characteristics, thermal behavior and the induced flow magnitude: thin electrodes result in enhanced EHD flows compared to thick electrodes resulting in increased mechanical efficiency (despite consuming more power) while thick electrodes result to higher surface temperature [3,16,17]. Commercialization of SDBDs in different applications, require more advanced fabrication techniques that can ensure optimal and long-lasting operation in application-specific configurations (which might require complex electrode shapes) while minimizing design faults and overall costs.

To date, such advanced fabrication techniques applied to SDBDs are rather limited. For instance, high-precision CNC machines can be employed to build sophisticated SDBD arrangements employing 3D cylindrical electrodes [18,19]. This allows for crafting circular electrode leading edges as low as 100 μm. However, electrodes must be manually glued/clamped to the dielectric surface afterwards which does not guarantee perfect adherence. Printed electronics and circuit board (PCB) techniques such as photolithography and wet/chemical etching have been used to generate more complex electrode designs such as the serpentine SDBD [20], able to generate three-dimensional flow features (compared to the quasi-two-dimensional flows emerged in linear-SDBDs). Millimeter size SDBDs have fabricated using a micro-electromechanical system (MEMS) process, achieving electrode thickness of 300 nm through a standard lithography process and vapor deposition of chromium/gold/chromium electrodes. A screen-printing technique is reported in Ref. [21]. These techniques, although very interesting and successfully demonstrated, are costly and require advanced facilities and know-how, require several steps and (often toxic) chemicals, while they hinder flexibility on material selection and pattern design. Recently, inkjet-based printed electronics technology has emerged as a promising technique for SDBD fabrication due to its low-cost process, ease of operation, design flexibility and availability of an increasing variety of commercially available conductive inks. Being a non-contact and no-mask printing and patterning method, it typically requires just two steps: printing and sintering. SDBDs fabricated by inkjet printing using silver ink [22–24], full-inkjet-printed SDBD [25] (where both electrodes and the dielectric are inkjet-printed have been reported. Despite its merit, standard inkjet printing (IJP) presents several drawbacks, such as the need for low-viscosity inks, weak suitability for non-planar thus variable material substrates, low-to-moderate resolution of printed line width (at least with non-exotic setups i.e. super inkjet technology) and nozzle clogging issues due to the direct, bulk ink flow through the nozzle.

Aerosol Jet Printing (AJP) is a promising alternative to the IJP technique to fabricate SDBDs. While both methods allow non-contact patterning (a huge advantage over mechanical methods), they differ in their working principles, material compatibility, resolution, and applications. AJP excels in precision applications requiring high resolution and material versatility. During AJP, liquid ink, containing materials such as functional nanoparticles and polymers, is atomized to produce droplets on a scale of 1–5 μm. After being transported to the print head by a carrier gas flow, the aerosol stream is constricted by an annular sheath gas before exiting through a nozzle. AJP provides high resolution due to its ability to produce fine aerosolized droplets and the use of a sheath gas, around the aerosol beam, allows for better control over deposition, resulting in more consistent line width and smoother edges compared to IJP [26]. Furthermore, it is less prone to clogging (the sheath gas protects the aerosolized ink from touching the inner side of the nozzle), while achieving higher conductivity when compared to IJP for the same sintering protocols [27]. The resulting process can print lines on the order of 10–100 μm wide with its "narrow" class of nozzles and printing lines on the order of 800 μm wide with the "wide" nozzle class [28]. The AJP technology is optimized for inks within a wide range of viscosity (i.e. 1–10 cP for ultrasonic atomization and 1–1000 cP for pneumatic atomization).

A detailed quantitative comparison between AJP, IJP and conventional methods (e.g. conductive tapes) is not straight-forward due to the dependence of Jet Printing methods on various parameters (e.g. selected ink, printing method, substrate, sintering conditions etc) as well as the variety of manufacturers and quality of conductive tapes. Below, we try to summarize the main characteristics, benefits and drawbacks of each method. AJP and IJP are direct-write, contactless, mask-less and perfect candidates for manufacturing low-cost and even flexible electronics with minimal waste. Both work with nanoparticle inks in liquid state that are deposited either by the drop-on-demand mode (DOD-IJP) for a smaller drop size and high placement accuracy or by the aerosolisation of the ink into dense mist (numerous droplets) by an inert gas under pressure (pneumatic AJP) or by ultrasonication (ultrasonic AJP). Overall, AJP and IJP have many similarities in terms of the deposited outcome with AJP excelling in higher resolution deposition, (a lot) wider range of printable inks and less often clogging. Conductive tapes and specifically the aluminum ones (used in this work) are manufactured usually by the Hall-Heroult process into foils, then pressure rolled into thinner films which are coated with a highly engineered pressure sensitive acrylic adhesive. In Table 1, we provide a comparison of AJP, IJP and traditional fabrication methods (using conductive tapes) in terms of key metrics relevant to SDBD actuators. We note that a detailed comparative study of AJP and IJP technologies for silver ink has been reported in [27].

In this work, we report for the first time (to the best of our knowledge) the fabrication of Aerosol Jet Printed SDBDs (AJP-SDBD) able to generate stable surface discharges and produce EHD flows. The structure of the remaining part of this article is as follows: In Section 2, we present the methods used for the fabrication and the characterization of the SDBDs. In Section 3, we present results on electromechanical characteristics. In Section 4, we discuss our results and some limitations/restrictions linked to the AJP technique. Last in Section 5, we conclude and provide future directions.

Table 1
Key metrics comparison of AJP, IJP and conventional fabrication methods.

Parameter	Direct-write printing technologies				Conventional methods
	AJP		IJP		Conductive tapes
Range of functional materials	– Conductive inks: Au, Ag*, C black, Cu, W, Pt, Graphene. – Dielectric (UV curable polymers, alumina), – Conductive polymers: PEDOT:PSS, – Semiconductors – Biomaterials. – Ag-C nanotubes (CNTs) – Ag nanowrires(AgNWs)		Same as AJP but in lower viscosity ranges.		Cu tape, Al tape.
Range of ink viscosity	1–1000 cP [29]		Typically, up to 2 cP, possible up to 25 cP [26,30]		Not applicable.
Deposition methods	Ultrasonic (u-AJP)	Pneumatic (p-AJP)	Continuous (CIJ)	Drop-on-demand (DOD)	None.
Tracewidth Resolution	~10um (ink dependent) [29]		Size of inkjet dots: > 50–60um [26,27].		mm range
Clogging	Print head specifically designed for minimal clogging (Optomec AJP technology).		First drop problem-i.e. often clogging of nozzle by dried ink.		Not applicable.
Adhesion characteristics	Additives into the liquid ink and sintering after deposition. Thus, ink dependent. No mid-layer needed – only metal-dielectric interface present. Adhesion properties depend on surface tension of the selected ink compared to the surface tension of the selected substrate and the sintering process (mainly temperature).				Resin, solvent based acrylic**, silicone, rubber. Metal-adhesive and adhesive-dielectric interfaces present. Very good/good adhesion dependent on substrate and manufacturer (5.5 – 10 N/m range**)
Edge sharpness	Lower edge sharpness compared to IJP due to the overspray effect [27].		IJP deposits droplets which are uniformly circular-shaped with high edge sharpness and no sprinkle splats or overspray but with higher diameter compared to the main splats in AJP. [27]		Slitting/ die-cutting dependent.
Thin film thickness	Hundreds of nm to few μm (depends on ink, nozzle diameter, motion stage speed, number of layers) [27,29]		Higher than AJP ([27] – see Table 1)		Manufacturer dependent. Typical values: 30–75um conductive foil + 50 – 100 μm adhesive
Coffee-ring effect	Applicable in both techniques resulting is less material in the center compared to the edge. [31]				Smooth layer in stripe.
Reproducibility	Excellent due to CAD based printing.		Excellent due to CAD based printing.		Moderate: Reproducibility depends cutting/shaping technique which hinders precision and complex designs.
Temperature resistance	Up to 300**°C [29] but ink & substrate dependent		Similar to AJP		-40–160°C** but model and manufacturer dependent
Clogging	Low/minimal owing to AJP technology.		First drop problem-i.e. often clogging of nozzle by dried ink. [31]		Not applicable.
Substrate compatibility	Nearly any substrate [32]: Flat and/or rough glass, plexiglas, flexible polyimide, paper, FR4, ceramic, stainless steel, Si wafer. It only depends on the application and ink compatibility. Specific models (e.g. Optomec's Aerosol Jet 300 Series) allow printing on 3D non-planar surfaces. [27,31]		Same as AJP but there is limitation for 3D non-planar surfaces.		Nearly any substrate.
Deposition velocity	In principle, higher in AJP. [27]		Lower in IJP due to the drop-on-demand mechanism. [27]		Not applicable.

* Silver Ink NovaCentrix Metalon JS-A426 used in this work.
** Tesa 60670 tape used in this work.

2. Methodology

2.1. Aerosol Jet Printing

The SDBDs were devised, designed and fabricated by CERTH, with an Aerosol Jet Printer (Optomec, AJ200 model) available at CERTH/CPERI and its ARTEMIS laboratory. The dielectric substrate used is commercially available Plexiglas (PMMA) with a thickness of 3 mm. An aqueous-based silver ink (Metalon JS-A426, NovaCentrix, USA) was used. The Metalon JS-A425 ink contains 50% w/w Ag nanoparticles, 30–40 nm in diameter, has a viscosity of 6–10 cP and is formulated specially for ultrasonic aerosolization. Additionally, it contains polyurethane binder

and is designed to present improved adhesion to variety of substrates such as paper, PET, glass and polyimide. Ultrasonic atomization (UA) is employed for all prints, with the aerosol carrier gas being pre-saturated, in a bubbler, with water vapor. A narrow circular nozzle (300 μm in diameter) was used for contouring, i.e., printing the exposed electrode edges (see below for details), while a wider nozzle (0.75 mm in diameter) was used for filling, i.e., printing the bulk areas of the electrode geometries. Both nozzles were delivered by Optomec Inc. (USA). During both contouring and filling stages, the same silver ink was used. The contouring step is important to be printed with the narrow type of nozzles as these produce significantly less overspray compared to the wide type of nozzles, a crucial parameter for the SDBDs as the electrode edge morphology dictates plasma ignition and stability. The two stage procedure significantly reduced the overall printing time (with respect to using only the narrow nozzle for the whole design). Curing/sintering was performed at 85 °C for one hour (adequate for the dielectric substrate – see below). Layers printed with the wide nozzle (filling stage) require an in-between step prior to sintering at which the deposited ink onto the substrate dries at room temperature for a minimum of two hours. The final assembly includes an additional dielectric layer (same thickness and material, i.e., 3 mm Plexiglas) glued (with Epoxy resin) to the bottom part of the actuator to create the SDBD sandwich structure and electrically insulate the bottom electrode, ensuring that plasma is ignited only on the top side. The epoxy glued SDBD was left to rest for more than 8 h at room temperature, to ensure proper curing. The whole procedure – from design to SDBD assembly – is subject to optimization and reduction in overall time required for a single SDBD print which falls outside the scope of this work. For the current work and dimensions (see below), a single AJP-SDBD print, excluding curing and drying stages, requires approximately 1–2 h. A schematic of the fabrication process and workflow is shown in Fig. 1.

2.2. Measurements of AJP ink resistivity and carrier properties

Prior to the SDBD fabrication, Van der Pauw and Hall-effect measurements have been conducted (at AUTH), at room temperature, to evaluate the values of specific resistance, charge carrier density, and mobility. A Van der Pauw experimental configuration attaining up to 0.5 T magnetic field strength was used, while measurements were taken for both magnetic field directions and current to eliminate voltage probe contact resistance effects as well as magnetoresistance contributions. Silver paint was used to form Ohmic contacts with an AJP rectangular electrode.

2.3. Plasma characterization

The AJP-SDBDs were initially tested in the Plasma Science and Innovations (PlaSci) research team of ARTEMIS laboratory in CERTH/CPERI, with an AC-HV generator delivering max output of up to 40 kV_{p-p} at 20 kHz in an open-air environment. More elaborated measurements including discharge power, Voltage-Current (V-I) waveforms and optical diagnostics were performed at LSPM/CNRS where the actuators were ignited by an AC-HV generator (Trek 20/20 C) triggered by a digital delay generator (Aim & Thurlby Thandar Instruments TG1010A). An HV probe (Cal Test CT4028, with an attenuation ratio 1000:1) was used to measure the applied voltage at the driven electrode, and a current transformer (Magnelab CT-D-2.5-BNC) was used to measure the discharge current in a digital oscilloscope with a sampling rate of 2.5 GS/s and a bandwidth of 1 GHz (Teledyne LeCroy HDO6104). The circuit included a capacitor (10 nF) to monitor the voltage drop across its terminals and register Lissajous curves in the oscilloscope, allowing direct calculation of the discharge power. For optical diagnostics, a Digital Single Lens Reflex (DSLR; Nikon D5300) camera and an intensified Charge Coupled Device (ICCD; Princeton Instruments PIMAX-1K-RB-FG-P43) were used to obtain time-integrated and -resolved images of the discharge. The DSLR camera was equipped with a VIS objective lens (Nikkor) and had the following settings to record the discharge emission: exposure time= 2 s and ISO= 400. The ICCD camera was equipped with a UV–VIS objective lens and allowed space-time-resolved monitoring of the plasma wavelength-integrated emission via suitable triggering from the delay generator. Furthermore, two spectrometers were used to acquire optical emission spectra of the discharge. The first was compact and portable (Avantes AvaSpec–ULS4096CL-EVO; 75 mm focal length, 10 μm slit size, 300 lines/mm diffraction grating, 4096-pixel CMOS linear image sensor) offering a low spectral resolution of ~0.5 nm/pixel for a spectral range of 200–1100 nm. In this case, the discharge emission was collected using a collimating lens (Avantes COL-UV/VIS) having an 8.7 mm focal length and fed into a quartz optical fiber bundle (Avantes FCUV400–2) coupled to the spectrometer's entrance slit. The second unit was a spectrograph (Oxford Instruments Andor Shamrock 500i) with 500 mm focal length, 100 μm slit size and three interchangeable gratings (1200, 1800 and 2400 lines/mm). This was coupled with an intensified sCMOS camera (Oxford Instruments Andor iStar sCMOS 18U-03). The nominal resolution for the spectra collected in the present work were 0.1 nm and 0.07 nm, for the 1800 lines/mm and 2400 lines/mm gratings, used for the estimation of the vibrational and rotational temperatures of $N_2(C)$, respectively. The discharge emission was imaged using a 2-inch UV lens (60 mm focal length) in a 2f–2f focusing configuration between the plasma and the entrance slit of the spectrograph. Both spectroscopic systems were calibrated in terms of relative spectral irradiance using a Halogen-Deuterium calibration lamp (Ocean Optics DH3-PLUS-CAL).

A schematic of the experimental setup is shown in Fig. 2. The operating conditions used for plasma characterization are shown in Table 2. It must be noted here that all measurements described in this work (OES, ICCD imaging, etc.) were performed after the AJP-SDBD had been

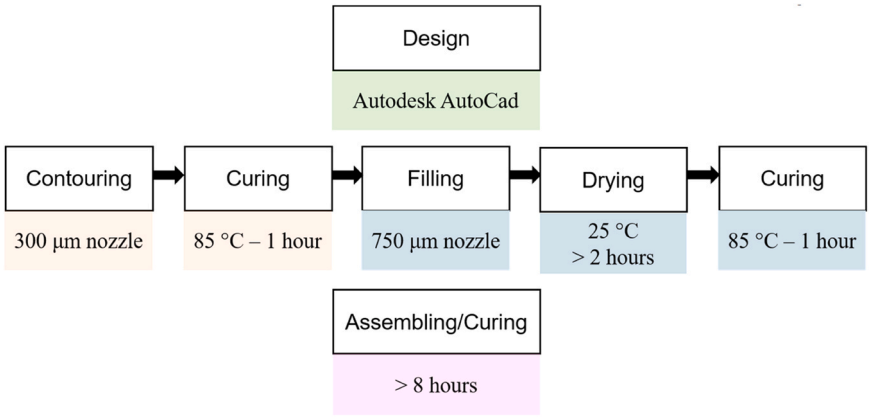

Fig. 1. Aerosol Jet Printed SDBD sequence and workflow.

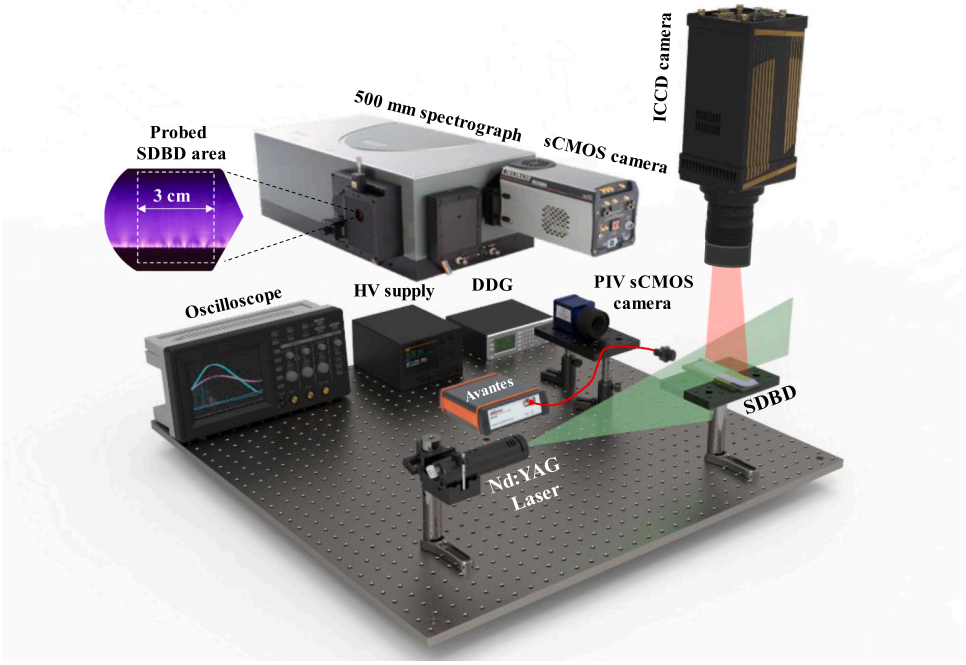

Fig. 2. Experimental setup of the different diagnostics applied. DDG stands for digital delay generator. The probed SDBD area by the high-resolution spectrograph is shown as an inset on the top side.

Table 2
Operating conditions for plasma characterization.

Plasma characterization	
Held Constant	*Varied*
$f = 3$ kHz	$V_{AC} = 12, 28, 30$ kV_{p-p}

Table 3
Operating conditions for flow characterization.

Flow characterization	
Held Constant	*Varied*
$f = 1$ kHz	$V_{AC} = 20, 25, 30, 35$ kV_{p-p}
$V_{AC} = 30$ kV_{p-p}	$f = 1, 2, 3$ kHz

operated for at least 15 min. This time was necessary for the device parts to reach thermalization and for the discharge properties (e.g., emission intensity of key species generated) to reach a steady state.

2.4. Ionic wind flow measurements and EHD body force reconstruction

Ionic wind measurements were conducted under quiescent conditions at the Low-Speed Lab of the Department of Flow Physics and Technology, at Delft University of Technology, using Particle Tracking Velocimetry (PTV). The actuators were enclosed in a Plexiglas box of 1000 × 500 × 500 mm dimensions, with sufficient optical access all around allowing external placement of the digital camera and the laser head. A LaVision Imager sCMOS camera (2650 × 2048 px), furbished with a 200 mm Macro lens captures the PTV images in double frame mode. The imaged region of interest of approximately 42 × 12.5 mm is illuminated by a Quantel Evergreen 200 Nd:YAG laser, used in a double pulse mode. The entirety of the enclosure was seeded using parafine-based particles (Shell Ondina) of approximately 1.5 μm average diameter produced by a TSI atomizer. The actuators were powered through Trek's 20/20C-HS high voltage amplifier (same generator used for the plasma characterization at CNRS), which is fed a digitally generated AC waveform from National Instrument's NI9215 card. An illustrative schematic of the experimental setup has been included in Fig. 2. The electrical parameters used for the ionic wind characterization are also shown in Table 3.

The acquired image pairs were processed using LaVision's DaVis FlowMaster 10.2 software to obtain the time-averaged flow field. Initial image pre-processing was applied to enhance particle visibility and consistency across the image datasets. The strong laser illumination produced a diffuse bright background, reducing contrast and complicating particle detection. To address this, the background intensity was normalized, reflections from walls and electrodes were removed, and the images were cropped to align the lower edge with the wall, thereby eliminating unwanted reflections from the base plate. These preprocessing steps ensured that the subsequent Particle Tracking Velocimetry (PTV) analysis could reliably identify and follow tracer particles throughout the flow domain.

Following image cleanup, the PTV algorithm was configured and executed to track particles between successive image pairs. The particle detection threshold, pixel size, and search window dimensions were optimized based on flow characteristics, with a 32 × 10 pixel window offset by 12 pixels in the streamwise direction to account for the dominant horizontal flow component, inherent to DBD plasma actuators. This setup allowed for the detection of both forward and reverse flow while minimizing false matches. The particle trajectories obtained from 1000 image pairs per case were then spatially averaged through a binning process, wherein the image domain was divided into 4 × 4 pixel bins. The velocity vectors within each bin were averaged to yield the time-averaged velocity field, while bins with insufficient data were excluded to suppress noise near walls. The final achieved vector resolution for the time-averaged velocity fields is 49 μm. The achieved vector resolution is examined in comparison to the characteristic half-height of the plasma induced wall jet at conditions $V_{pp} = 30$ kV and $f = 3$ kHz. The jet characteristic half-height is extracted at location of maximum velocity ($x = 7.1$ mm) and is found to be $y_h = 1.4$ mm, where $U(y_h) = 0.5\ U_{max}$.

The PTV measurements are used to aggregate the time-averaged flow field resulting from the operation of the SDBD actuators. Access to the mean velocity provides the opportunity for further characterization of

the volume-distributed body force generated by the plasma cloud [33]. The differential form of the Navier-Stokes equations is used, following the approach by Kriegseis et al. [34]. More specifically, the incompressible, steady form is considered as the velocity field is time-averaged and no time data is available (plasma interaction/momentum transfer is quasi-static).

$$\rho\left(u\frac{\partial u}{\partial x} + v\frac{\partial u}{\partial y}\right) = f_x - \frac{\partial p}{\partial x} + \mu\left(\frac{\partial^2 u}{\partial x^2} + \frac{\partial^2 u}{\partial y^2}\right)$$

$$\rho\left(u\frac{\partial v}{\partial x} + v\frac{\partial v}{\partial y}\right) = f_y - \frac{\partial p}{\partial y} + \mu\left(\frac{\partial^2 v}{\partial x^2} + \frac{\partial^2 v}{\partial y^2}\right)$$

where ρ is the density, u and v are the x and y velocity respectively, x and y are the directional grid spacing, f_x and f_y are the horizontal and vertical body forces, p is the pressure and μ is the viscosity. Following the approach by Wilke [35] assumed the pressure gradients to be negligible compared to the respective forces, as further confirmed numerically by Benard et al. [36]. With two equations and two unknowns, the respective body force components can be found. The time-averaged PTV velocity field retains some noise which can lead to unphysical spikes while computing the derivatives. Therefore, the u and v fields are smoothened by using 4th order bivariate spline surfaces fit to the respective velocity fields. The algorithm is based on the work of Dierckx [37], where spline functions are fitted to data on a rectangular grid using a least squares method.

Uncertainty in the time-averaged velocity fields extracted from PTV measurements is estimated to be approximately 0.1% of the maximum plasma-induced velocity [38]. Finally, it must be noted that the body force estimation method is inherently based on a 2D projection and as such can result in significant errors if the measured flow field exhibits strong out-of-plane components. To mitigate this, the PTV plane was aligned to the mid-span of the actuator. Considering a characteristic induced jet half-height in the order of about 1 mm, and the spanwise extent of the actuator of 80 mm, edge effects on the PTV measurements are deemed negligible. Furthermore, the uncertainty in the time-averaged velocity fields (~0.1% of U_{max}) is propagated through the body-force estimation method and provides an estimate of uncertainty for the calculated body force fields of approximately 0.5% of maximum body force.

3. Results

3.1. Aerosol Jet Printed SDBD and printed electrode electrical properties

The linear AJP-SDBD was printed with no overlap or gap between the HV (top) and ground (bottom) electrodes. Using fiducial markers, an excellent alignment between the top and bottom printed electrode has been achieved. Conductive paths to allow for proper connection with the HV power source and ground terminals have also been printed. The design as well as dimensions is shown in Fig. 3, where W_1= 80 mm, L_1= 15 mm, L_2= 20 mm, D_1= 20 mm. In this schematic, the regions that have been printed with the narrow nozzle (for contouring) and the regions printed with the wide nozzle (for filling) are shown in different colors. The width of the contouring regions is 1 mm. Another piece of dielectric (same thickness and material i.e. 3 mm Plexiglas) has been glued (with epoxy resin) to the bottom part of the actuator to create the sandwich structure and electrically insulate the bottom electrode.

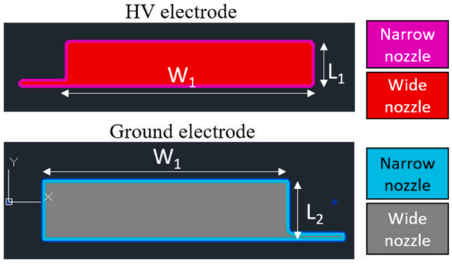

Fig. 3. Linear AJP-SDBD – schematic and dimensions.

The trace width of the JS-A426 silver ink using a 300 μm diameter nozzle is approximately 80um, with minimal overspray, while, when using a 0.75 mm diameter circular wide nozzle, it is approximately 400–500 μm with ~50 μm overspray on each side. The thickness of the deposited layer (printed with the narrow nozzle) is approximately 4 μm (measured by a stylus profilometer). Resistivity, charge carrier density and mobility values extracted from Hall measurements are shown in Table 4, for samples that have been printed in x, y, and 45°/135° directions. Considering that the measurements show homogeneous structures, the lower resistivity values are attributed to a high-quality print result. Overall, the three electrodes show a metallic behavior, with their electronic properties comparing very favorably to other printable materials like PEDOT:PSS (1 – 10^{-2} Ωcm) or graphene ink (3–8 $\times 10^{-3}$ Ωcm).

Fig. 4 shows different phases of the printing process. On the right side, the final linear AJP-SDBD print is also shown. The regions of contouring and filling are reflected on the ink structure and are visible with the naked eye. Fig. 5 shows images acquired with a microscope (Motic, SMZ-168-BL) showcasing two different regions of the top (exposed) electrode edge (where the plasma forms). On the left, a region near the middle of the SDBD length is shown, which demonstrates the fine quality of the printing at this critical area. On the right, an image at the utmost right edge of the top electrode is shown, which demonstrates the smooth curvature of the print, and which was used to reduce non-desirable edge effects at this region.

3.2. Plasma characterization

Fig. 6a, and b show the V–I characteristics and corresponding Lissajous curves of the AJP-SDBD operating at different peak-to-peak (p-p) applied voltages: 12, 28 and 30 kV_{p-p}. The corresponding current waveforms in Fig. 6a exhibit typical DBD behavior under AC excitation: numerous narrow and rather erratic pulses are captured for all applied voltages being superimposed to a weak capacitive current component. These electrical characteristics agree well with the two-phase operation of typical AC-SDBDs [1,39]: during the positive-going phase of the AC waveform ($dV/dt > 0$), the (positive) current pulses are higher in peak-amplitude and correspond to streamers that propagate on the dielectric surface. During the negative-going phase ($dV/dt < 0$), the pulses are more numerous but lower in amplitude and correspond to a pulsating glow-like micro-discharge formation. As the applied voltage increases from 12 to 30 kV_{p-p}, the number and amplitude of current impulses also increases, due to an enhancement of the local electric field and more efficient gas breakdown and air ionization. Similarly, the area of the Lissajous plots in Fig. 6b significantly increases with increasing voltage, reflecting a higher energy dissipation into the plasma. Table 5 shows the power consumption which generally ranges in the 0.1–1 W/cm range, in agreement with previous studies (see for example Ref. [40] where a 3 mm dielectric was used).

For comparison with conventional hand-made SDBDs, Fig. 6c and d, present the features of the AJP-SDBD under the same operating conditions (30 kV_{p-p}, 3 kHz) with those of a hand-made SDBD using tape electrodes (called “taped” SDBD). For the latter, we’ve used aluminum

Table 4
Resistivity, charge carrier density and mobility of mono-axial x, y and criss-crossed printed electrodes.

	x-axis	y-axis	x-y
Resistivity (Ωcm)	$1.5\ 10^{-4}$	$3.4\ 10^{-4}$	$1.4\ 10^{-4}$
Charge carrier density (cm^{-3})	$1.5\ 10^{23}$	$5.5\ 10^{22}$	$7.6\ 10^{22}$
Mobility (cm^2/Vs)	0.3	3.4	0.6

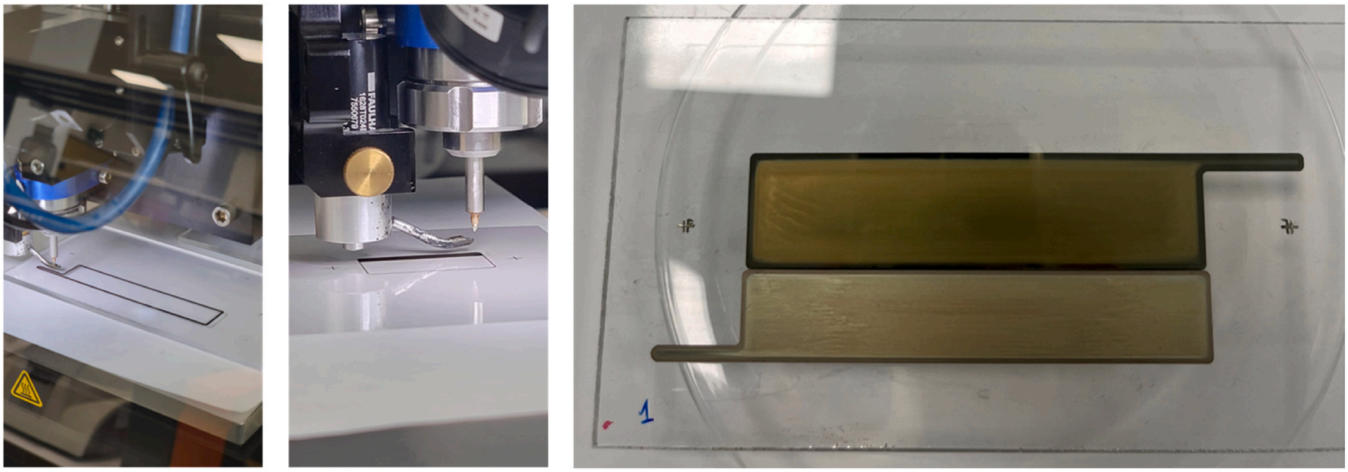

Fig. 4. Linear AJP-SDBD - images of printing process (left, middle) and final print where both top and bottom electrodes are visible (right).

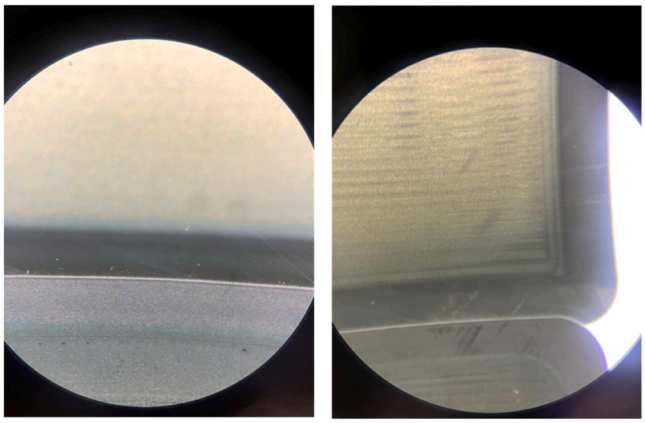

Fig. 5. Microscope images of the top electrode edges. Left: linear region corresponding to the middle of the SDBD length. Right: Curved edge region corresponding to the utmost right edge of the top electrode.

tape (tape thickness: 80 μm) for the electrodes, cut in similar dimensions as the AJP-SDBD, and exactly the same Plexiglas (dielectric) substrate with the AJP-SDBD. The taped SDBD seems to produce fewer current spikes and, thus, discharge events, than the AJP-SDBD, which is consistent with the differences observed in the optical emission features between these devices (see below). Indeed, an accurate quantification of the number of current spikes in Fig. 6c(i) and c(ii) gives an average of approximately 150 ± 20 impulses for the taped SDBD and 353 ± 14 spikes for the AJP-SDBD per positive half-cycle (calculated over three consecutive periods), i.e, the AJP-SDBD produces about two times more impulses than the taped SDBD. We note that the temporal resolution of the oscilloscope used (sampling rate of 2.5 GS/s (0.4 ns time resolution), high vertical resolution (12-bit)) is more than sufficient to resolve individual current pulses and distinguish them from noise. To demonstrate this, In Fig. 6(d) we show a zoomed-in view of the current waveform, where the individual pulse shapes are clearly resolved and the difference on the pulse number between the taped and AJP-SDBD is clearly seen. This denotes that AJP-SDBD is more advantageous due to a much more efficient power transfer and plasma formation. Indeed, if we consider the corresponding Lissajous loops (Fig. 6d), the dissipated power for the hand-made SDBD is 2.41 W (0.3 W/cm – in excellent agreement to the results in Ref. [40] – Fig. 5, where a 80 μm thick electrode was used) while for the AJP-SDBD it is 5.98 W (0.747 W/cm), i.e., ~2.5 times larger which resembles their difference revealed in the number of current pulses. This discrepancy is attributed to the finer electrode contour, and reduced thickness of the AJP electrode (approximately 4 μm), which enhances the local electric field and promotes more efficient ionization along the driven electrode's edge. To verify our claim, we have performed 2D electrostatic simulations of the exact SDBD geometry (including the dielectric layer) using the Poisson solver from the in-house plasma solver COPAIER, which has already been used to study linear and annular SDBDs [39,41]. We compare two different electrode thicknesses: one of 4 microns (corresponding to the AJP actuator) and one of 75 microns (corresponding to the thickness of the conductive strip from the aluminum tape used in this study). Fig. 7 shows the electric field magnitude contours for both cases, normalized to the maximum field value obtained for both electrode thicknesses. The electric field distribution is quite different in the two cases: the thin electrode results to a maximum field of approximately 20% higher, while the field is highly concentrated near the right edge, presenting a rather spherical profile. With the thick electrode, the E field distribution is quite different, presenting two zones of high fields near the two corner points of the electrode vertical edge, while the highest values are present at the bottom corner (electrode – dielectric – gas triple point). These results indicate a more efficient breakdown in the thin (AJP) electrode case owing to the higher field values. We also note that for the case of thick electrodes and during the positive phase, streamers typically initiate from the top electrode corner as shown in self-consistent simulations [39] (due to the direction of the electric field vector and corresponding directional charge drift). At this region, the electric field is even weaker (60 – 70% lower than the maximum electric field in the thin electrode case) which indicates that breakdown and discharge ignition might be even more pronounced with thin electrodes. Last, the sheath thickness at atmospheric pressure and at high plasma density ($\sim 10^{20}$ m^{-3} as shown in the simulations) can be quite small (less than 50 μm), affecting the negative phase which corresponds to the formation of numerous microdischarges burning near the exposed electrode: at the thin electrode case, the whole electrode edge is surely involved in the sheath dynamics. To further verify these initial results, self-consistent plasma simulations are necessary, which are planned for future work. Furthermore, the AJP electrode adheres much better to the dielectric surface, limiting air bubble trapping between it and the surface of the Plexiglas, thus significantly suppressing parasitic discharges and maximizing power transport to the surface discharge.

Fig. 8 shows representative images of the AJP-SDBD taken with the conventional DSLR camera under various operating conditions. They show the global discharge morphology around the driven electrode. At higher applied voltages at constant frequency (left and middle images), the plasma emission significantly intensifies and seems to spread more uniformly along the electrode and further downstream on the dielectric surface. At lower frequency and constant applied voltage (middle and

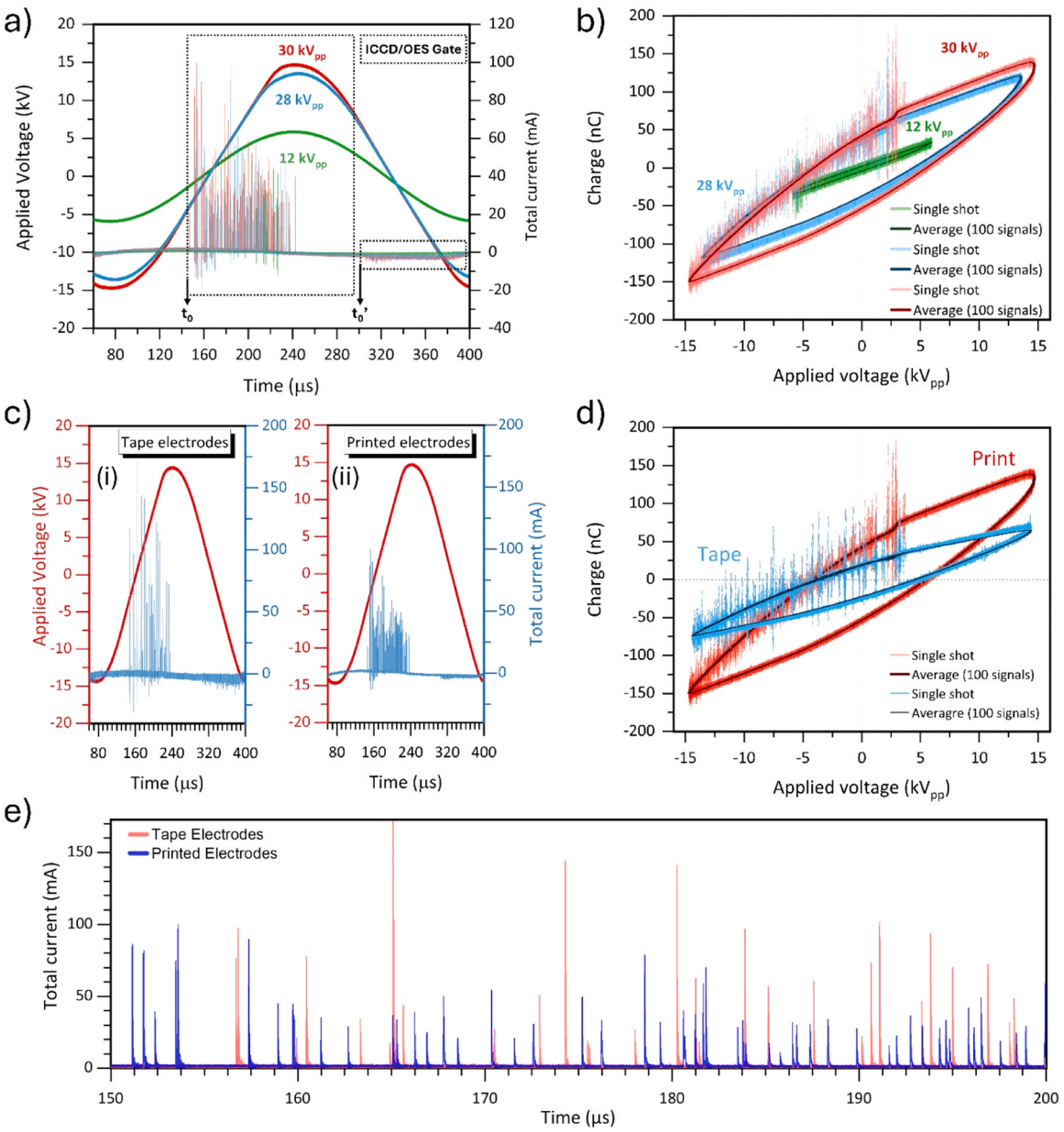

Fig. 6. a) VI characteristics for different applied voltages at f = 3 kHz. The instants t_o and $t_o^{'}$ denote the start of the ICCD gate delay used to capture the time-resolved discharge evolution during the rising and falling AC voltage phases; the dashed rectangles denote the gate widths used to capture time-integrated discharge dynamics during both AC voltage phases. b): Lissajous curves for same conditions with a). c) VI characteristics of hand-made taped (i) and AJP (ii) SDBDs at V_{p-p}= 30 kV and f = 3 kHz. d) Lissajous curves for taped (blue) and AJP (right) SDBDs at V_{p-p}= 30 kV and f = 3 kHz. d) Comparison of current waveforms in the temporal range 150–200 μs, corresponding to the waveforms of (a) for the taped and AJP SDBDs at V_{p-p}= 30 kV and f = 3 kHz.

Table 5
Electrical power consumption of AJP-SDBD.

	3 kHz - 12 kV_{p-p}	3 kHz - 28 kV_{p-p}	3 kHz - 30 kV_{p-p}
Normalized Power (total power)	0.022 W/cm (0.178 W)	0.545 W/cm (4.36 W)	0.747 W/cm (5.98 W)

right images), the discharge emission weakens and the plasma glow is more concentrated near the exposed electrode. In all cases noticeable edge effects are seen with curved emission lines at the right and left sides of the driven electrode, following the lines of the electric field.

We now focus on the V_{p-p}= 30 kV and f = 3 kHz case and present time-averaged and single-shot ICCD images (Fig. 9a,b) which provide deeper insight into the discharge spatiotemporal development within the rising and falling AC voltage phases as well as the full AC cycle. The ICCD settings were set as follows: 150 μs delay (see t_o in Fig. 6a) and 150 μs width for the rising phase; 310 μs delay (see $t_o^{'}$ in Fig. 6a) and 150 μs width for the falling phase; 150 μs delay and 300 μs width for the full cycle. Fig. 9a (rising AC phase) shows intense discharge spots starting from the electrode's edge and spanning its entire length. These seem to quickly transform into a uniform discharge propagation away from its edge. A rather different behavior is seen in the falling AC phase; the initial channels at the electrode's edge appear to be brighter and the discharge pattern away from it seems to be fainter. The 3 mm scale bar in the figure confirms the micro-scale nature of the discharge, typical for surface DBDs operating at atmospheric pressure. Although these analyses offer more details compared to the DSLR camera, a clearer idea on the true structure of the discharge's emission can only be obtained using single-shot ICCD imaging (Fig. 9b). Indeed, Fig. 9b(i,ii) clearly shows a

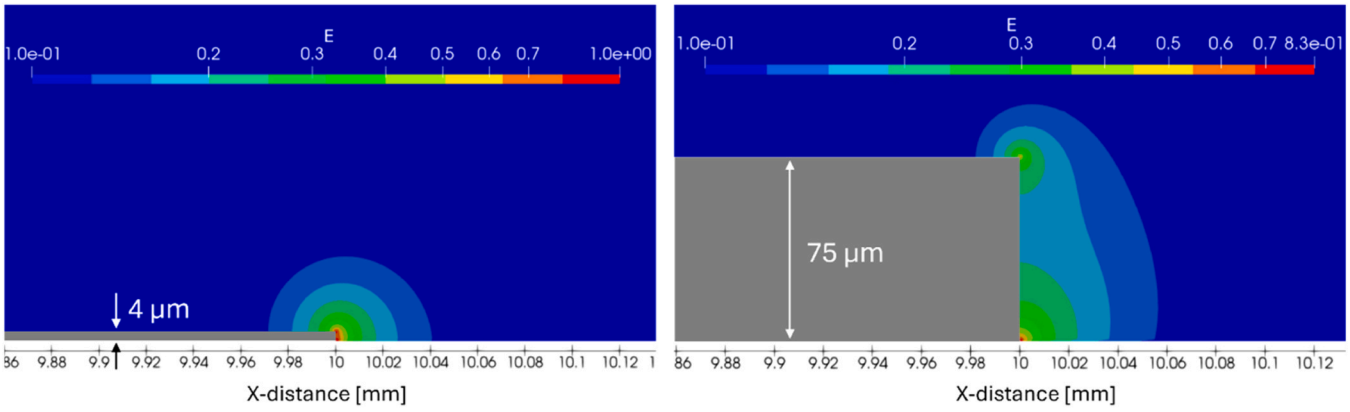

Fig. 7. Electric field magnitude contours for HV electrode thickness of 4 μm (left) and 75 μm (right). Log-scale – normalized to the maximum field value for both cases.

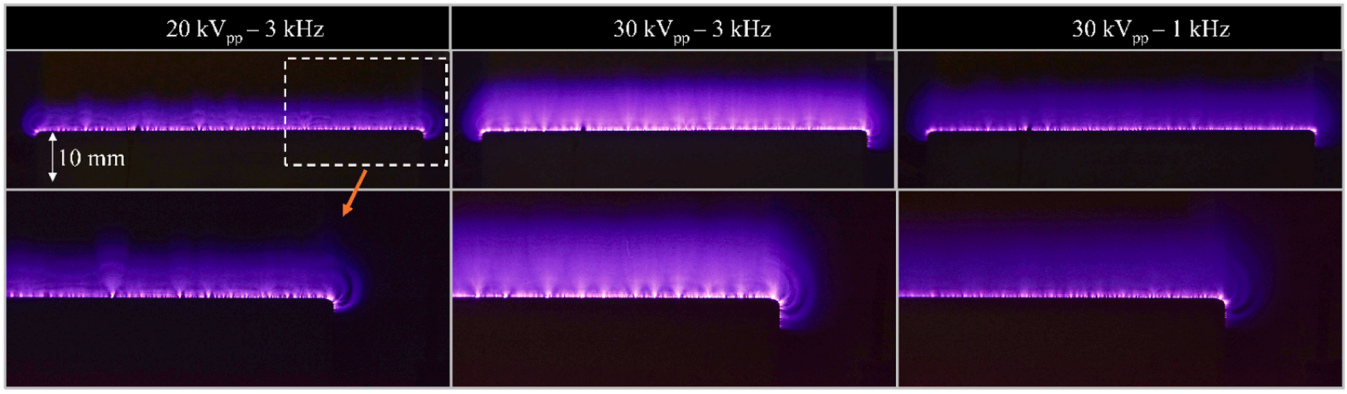

Fig. 8. DSLR images (exposure time=2 s and ISO=400) of the AJP-SDBD under different operating conditions. Top: full scale images. Bottom: zoom at electrode's right edge.

rich diversity of filamentary patterns during the rising voltage phase due to positive streamers that stochastically propagate along the dielectric surface. These extend over a distance of about 10 mm away from the driven electrode exhibiting noticeable branching, curling, and bifurcation. These filamentary structures suggest non-uniform electric field distribution, surface charge accumulation and resulting electrostatic repulsive forcing, all characteristic of AC-driven SDBDs [42]. During the falling AC phase, as seen in Fig. 9b(iii,iv), however, short distinct channels remain attached to the driven electrode's edge while further upward the discharge exhibits a glow-like behavior, leading to a more homogeneous pattern across the dielectric surface. This phase is characterized by microdischarge formation very close to the exposed electrode due to the potential different of the previously positively charged section of the dielectric surface (note that this section is typically adjacent but not connected to the electrode [39]) and the now negative applied potential on the exposed electrode. Each microdischarge which corresponds to a current pulse, takes the form of a short and thin quasi-neutral plasma that connects to the exposed electrode. It then results to a relaxation phase with strong electron drift away from the exposed electrode neutralizing and charging negatively the nearby dielectric section. These electrons lead to the formation of ion clouds (via electron impact ionization and attachment) and during each subsequent pulse, the process repeats and the space charge volume is continuously extended further downstream. The elongation of this space charge region during the negative-going phase is linked to the streamer extension and related dielectric charging during the positive-going phase. These AC-related plasma regimes in SDBDs and corresponding physics of streamers and microdischarge formation have been studied extensively in the past years (see [39,43,44]) and a detailed analysis falls outside the scope of this work. Finally, Fig. 9b(v,vi) represents superposition of the discharge events formed in the previous two phases with dominant contribution from the rising phase away from the driven electrode, and from the falling phase at the close vicinity of the electrode. Overall, Fig. 9 effectively captures the asymmetric nature of streamer propagation in AC sinusoidal excitation, where both positive and negative half-cycles contribute differently to discharge morphology. The presence of distinct three-dimensional filamentary structures and propagation paths implies strong surface-discharge coupling and showcase the increased intensity of the positive-going phase plasma regime.

The dynamics of these different plasma regimes are shown in Fig. 10, which depicts time-resolved ICCD images of the discharge evolution during the rising (Fig. 10a) and falling (Fig. 10b) AC voltage phases. Despite the stochastic nature of the discharge development, these results shed bright light on the chronological order of the corresponding patterns previously observed in Fig. 9a and b. It should be noted that the numerous discharge events formed during both phases are representative of the current pulses shown in Fig. 6a. Fig. 10a shows the early stages of discharge formation in the rising AC part, revealing bush and glow-like structures at 163 μs which densify at 166 μs and start to elongate after 178 μs. Besides, after 196 μs, these transform into branched/curled filaments, the density of which significantly increases until around 220 μs, just before they reach their maximum propagation length (at 235 μs). Then, they seem to maintain their length until 255 μs (i.e., when the peak voltage is attaint; see Fig. 6a); however, their density noticeably decreases between 235 and 255 μs and they totally

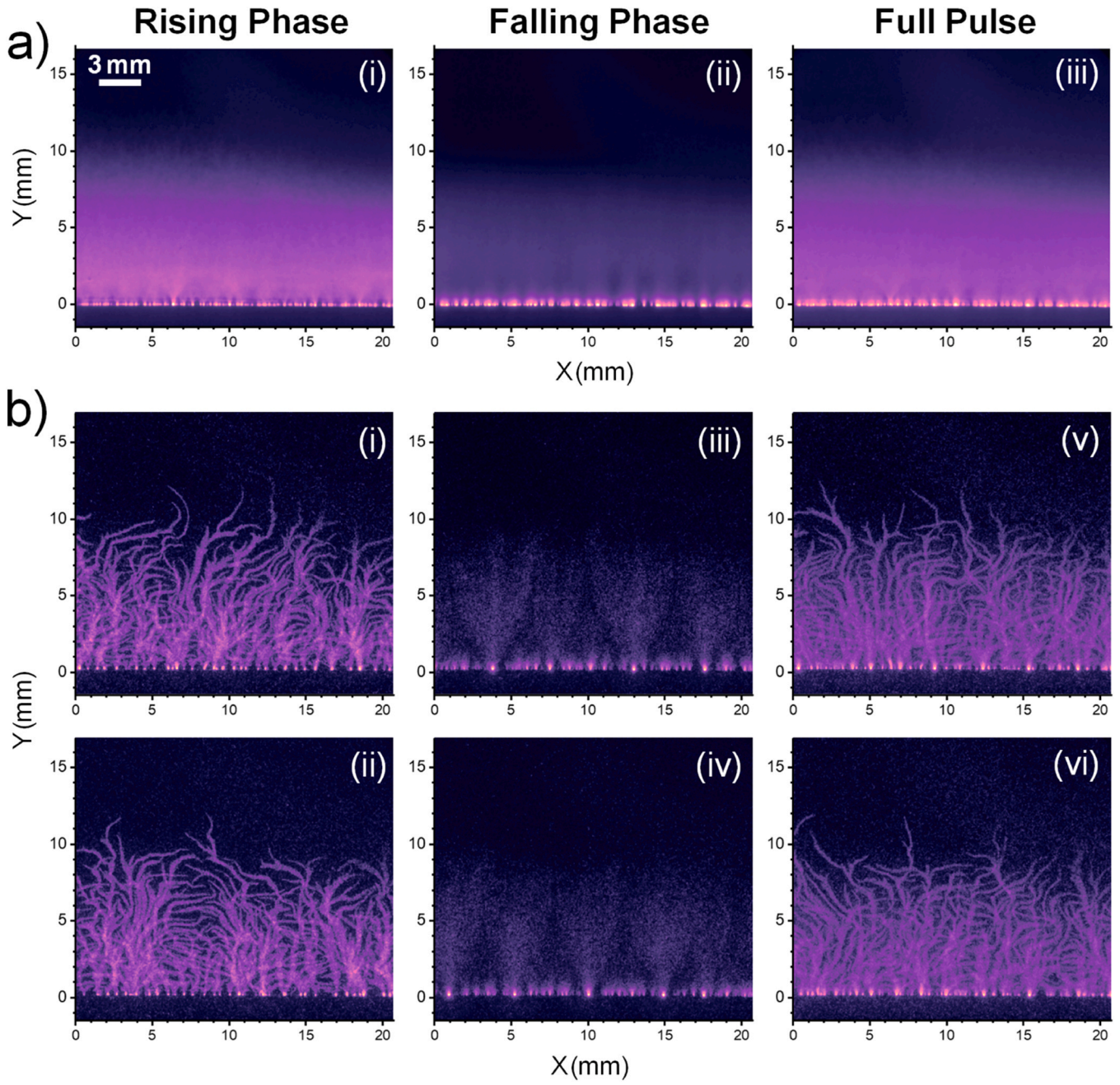

Fig. 9. a). ICCD images (500 single-shot frames averaged through post-processing) of discharge structure over a small selected AJP-SDBD area at $V_{p\text{-}p}$= 30 kV and f = 3 kHz. (i): Rising AC voltage phase. (ii): Falling AC voltage phase. (iii): Full AC voltage cycle. b) Indicative single-shot ICCD images of discharge structure at $V_{p\text{-}p}$= 30 kV and f = 3 kHz. (i-ii): Rising AC voltage phase. (iii-iv): Falling AC voltage phase. (v-vi): Full AC voltage pulse (see Fig. 5a for a time correlation with the voltage waveform).

disappear after 262 μs. It is remarkable that these filaments initiate from (or very close to) the exposed electrode and propagate on the dielectric surface without being detached from their initial starting point. The appearance of thin, bright and sharp filaments denotes enhanced localized electron densities and energy deposition which are characteristic of typical streamer heads. During this positive going phase, the EHD production is mainly attributed to the relaxation phase of the streamer formation i.e. the time periods between each high-current pulse where quasi-neutrality is broken [45]. Fig. 10b shows the initial discharge phases during the falling AC voltage phase. Here, the first plasma structures appear at the edge of the driven electrode at around 316 μs and start to intensify until 330 μs without any noticeable length change, indicating a glow-like regime until this time-instant. Their length significantly increases only after 360 μs and continues to increase until around 430 μs indicating that during this time period, micro-discharge formation and electron/ion cloud expansion occurs as described above. At 430 μs the discharge becomes practically invisible, the AC voltage reaches the minimum value, and the discharge stops after 441 μs. The discharge pattern in this case noticeably differs from that shown in Fig. 10a. As expected and as described above, the discharge shows a general glow-like behavior, being more diffuse and uniform with absence of filaments and broader vertical span. The maximum propagation length of the space charge cloud in this case is similar to the positive-going phase (almost 10 mm), as expected by the interconnection of the remnant positive surface charge during streamer propagation and necessary electric field enhancement for microdischarge formation

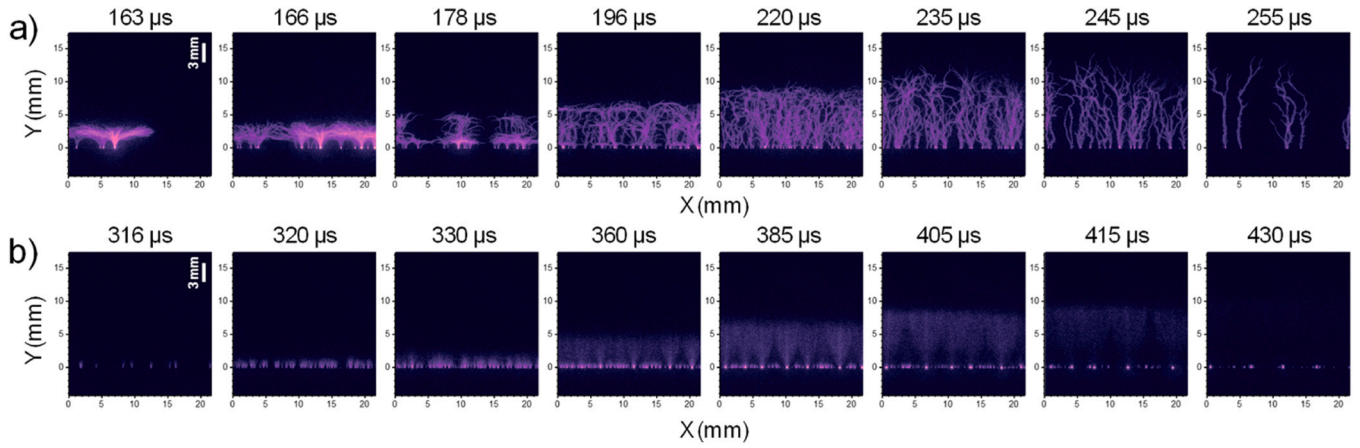

Fig. 10. Time-resolved ICCD images of the discharge evolution during a): rising AC voltage phase, b): falling AC voltage phase, at $V_{p\text{-}p}$= 30 kV and f = 3 kHz. These are captured using 1 μs gate width and 100-frame accumulation. The gate delay is shown in the images starting from t_0= 150 μs (upper frames; see Figure 5a) and $t_o^{'}$= 310 μs (lower frames; see Fig. 5a).

and electron drift downstream on the dielectric. During this phase, negative ions are expected to play the most significant role in the production of EHD force and ionic wind [43,46].

Fig. 11a shows the time-averaged low-resolution emission spectrum of the AJP-SDBD plasma in air at 30 kV_{pp}, 3 kHz. It highlights the primary excited species formed. The spectral region 280–450 nm is dominated by molecular nitrogen bands of the Second Positive System of $N_2(C^3\Pi_u \rightarrow B^3\Pi_g)$. Also, emission from the First Negative System of $N_2^+(B^2\Sigma_u^+ \rightarrow X^2\Sigma_g^+)$ is detected with its characteristic band at 391.4 nm. These emissions indicate that electrons in the discharge are exciting ground state N_2 molecules to the $C^3\Pi_u$ state and can also ionize N_2 to form $N_2^+(B)$, consistent with a typical air DBD plasma [47,48]. The prevalence of N_2(SPS) bands (and the relative absence of other species commonly found in air plasmas like excited atomic oxygen) confirms that most of the deposited energy goes into electronic excitation and/or ionization of molecular nitrogen. Fig. 11b demonstrates the stability of the SDBD emission features over time by tracking the peak intensities of selected N_2(SPS) and N_2^+(FNS) transitions (at 337.1 and 391.4 nm; see Fig. 9a) over a 40-minute period. After about 10–15 min of continuous operation both emission intensities remain steady within the experimental uncertainty, highlighting the robustness of the plasma generated by the AJP-fabricated electrodes. Therefore, all measurements shown in

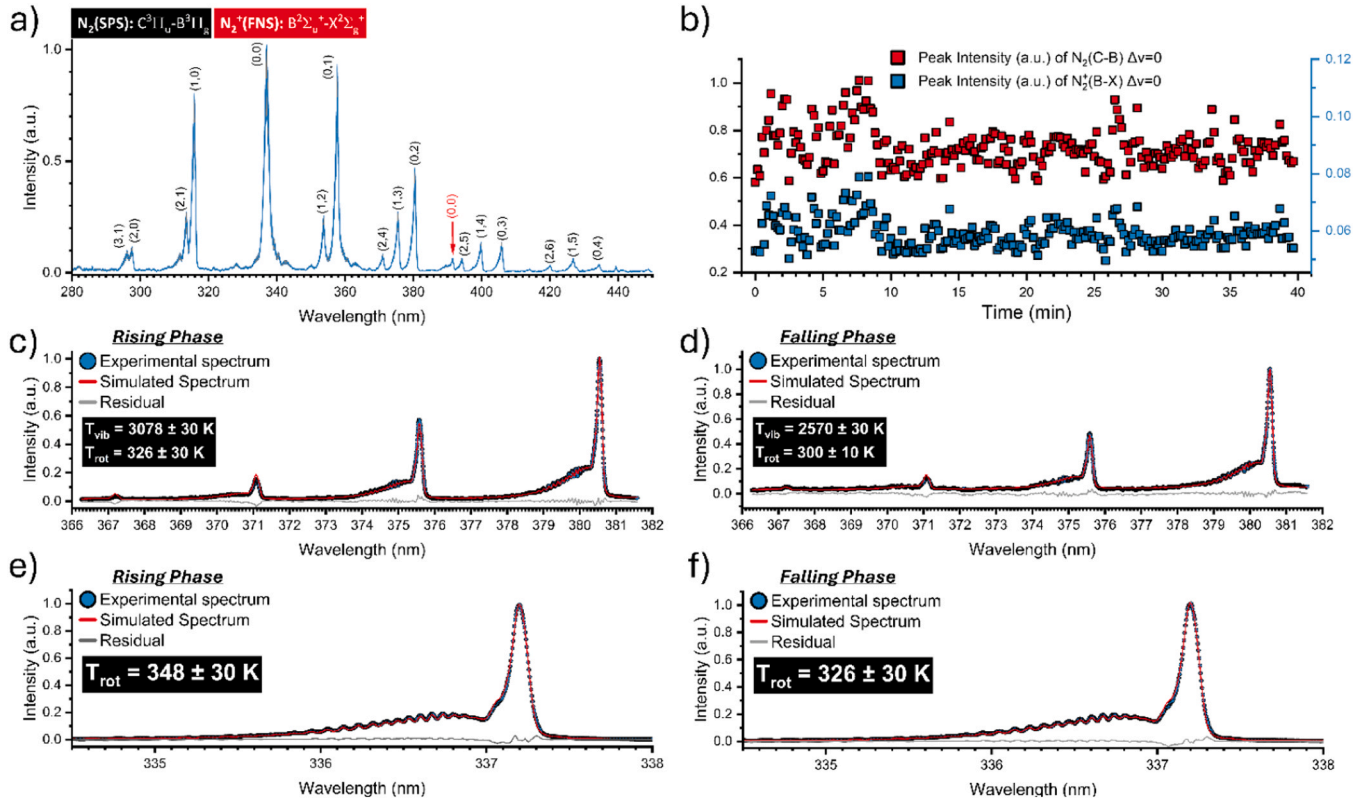

Fig. 11. a) Wide emission spectrum of AJP-SDBD (Vpp=30 kV and f = 3 kHz) with the key species detected. b) Intensity evolution of N2(SPS) and N2 + (FNS) during the first 40 min after the discharge's ignition. c,d,e,f) Experimental ro-vibrational spectra (blue) of N_2(SPS) during the rising (c,e) and falling (d,f) AC voltage phases. These are fitted with synthetic spectra (red) to determine the vibrational (c,d) and rotational temperatures (e,f) of N_2(C). The gating conditions were set as follows: 150 μs delay (t_o in Fig. 5a) and 150 μs width for the rising phase; 310 μs delay ($t_o^{'}$ in Fig. 5a) and 150 μs width for the falling phase.

this work (OES, ICCD imaging, etc.) were performed after the AJP-SDBD had been operated for 15 min. It should be noted that the actuator demonstrated its ability to maintain stable operation during the short-term experimental windows studied in this work, corresponding to more than 30 million AC cycles of operation. Thus, the robustness of the AJP-SDBD was evaluated by monitoring the discharge stability over rather short operation periods (<3 days). For example, the time-resolved ICCD imaging and the OES stability tests required approximately 40 min of continuous operation at 3 kHz. This corresponds to a cumulative load of over 7 million high-voltage cycles per experiment. Throughout these periods, accumulating more than 10^7 cycles, the actuator exhibited no signs of dielectric breakdown, electrode detachment, or intensity drift.

Using the high-resolution spectrograph, quantitative information was obtained about plasma rotational and vibrational temperatures. This was also achieved through a more detailed analysis of ro-vibrational spectra of selected spectral bands. First, time-averaged spectra of N_2(SPS) during the rising and falling phases of the AC voltage cycle were approximated with simulated spectra (using the MassiveOES software [49–51]) in order to determine the corresponding vibrational (T_{vib}) and rotational (T_{rot}) temperatures of N_2(C). The reported uncertainty values for T_{vib} and T_{rot} account for the experimental signal-to-noise ratio and the sensitivity of the fitting procedure. Specifically, they represent the temperature interval within which the residual sum of squares between the measured and simulated spectra remains comparable to the experimental noise level. The spectral resolution of the spectrometer may also play a role on the accuracy of the obtained values. The highest the spectral resolution is the better the accuracy of the measured T_{rot} and T_{vib} will be. This is of course valid until a separation limit between adjacent rotational lines is distinguished (typically on the order of few 10 s pm or smaller). To achieve a good spectral resolution, a monochromator with high focal length (ideally 2 m [52]) is required, which is not currently available in our case. However, the spectral resolution of our spectroscopic system, is still acceptable to have a good estimation of the T_{rot} and T_{vib}, given also the fact that we perform measurements during the positive and negative phases of the AC voltage. Making an accurate estimation of the uncertainty of our measurements compared to those made with a higher resolution spectrometer is not straightforward. This would require a direct comparison of the fitting result of the same ro-vibrational band recorded with higher and lower spectral resolutions. Thus, we can only estimate a total uncertainty of the temperatures on the order of 10–15% of the values provided by the fitting. The fitted spectral regions correspond to the $\Delta\nu$= -2 ro-vibrational band of N_2(C-B) (Fig. 11c,d) and the $\Delta\nu$= 0 (ν'=0→ν''=0) rotational band of N_2(C-B) at 337.1 nm (Fig. 11e, f). In the rising AC voltage phase (Fig. 11c,e), the inferred values indicate a $T_{vib} \approx 3078 \pm 30$ K, while the rotational temperature remains almost an order of magnitude smaller ($T_{rot} \approx$ 326–348 K). This decoupling of vibrational and rotational modes reflects the non-equilibrium nature of the discharge, in agreement with other similar studies performed in atmospheric pressure plasmas [48,53]. The elevated T_{vib} values are consistent with the presence of intense streamer channels observed in the ICCD images, which accelerate electrons to energies large enough for efficient vibrational energy transfers. During the falling phase (Fig. 11d,f), a reduction in vibrational temperature is observed ($T_{vib} \approx 2570 \pm 30$ K), while the rotational temperature is fairly similar ($T_{rot} \approx$ 300–326 K). This trend suggests that at the falling AC voltage phase, the energy available for electron impact processes is reduced, resulting in fewer vibrational excitations [53,54]. As a matter of fact, the discharge mechanism is not the same during the rising and falling AC voltage phases: in the former case we deal with positive (cathode-directed) streamers with electrons moving towards the driven electrode and inducing gas excitation/ionization; in the latter case, we deal with microdischarges near the electrode, electron drift away from the electrode and ion production during a charge relaxation phase, leading to weaker excitations and more diffuse emission pattern. The rotational temperature across both phases is quite similar which confirms that the bulk gas remains near ambient conditions, indicative of a non-thermal plasma device. Therefore, gas heating is not expected to play a key role in the modification of flow dynamics. While a detailed kinetic analysis is beyond our scope, the key point to retain from this OES analysis is that the AJP-SDBD generates the same types of emissive species as conventional SDBDs, while the extracted ro-vibrational temperatures align with literature values for common SDBDs [48], confirming that the novel fabrication method does not alter the fundamental plasma characteristics.

3.3. Electrohydrodynamic flow

Fig. 12a shows a typical contour plot of the induced jet's velocity magnitude, overlaid with velocity vectors. The plots shown are for the linear actuator operating at V_{AC} of 30 kV_{p-p} and f_{AC} of 3 kHz, which produced the highest induced velocity among the considered cases. The top electrode's edge is at x = 0 mm, and the ground electrode extends to x = 20 mm. Characteristic of a linear DBD actuator, a wall parallel jet is induced by the discharge, as can be seen by the domination of the horizontal velocity component. This wall jet is preceded by a region of downward velocity motion, seen as a non-negligible negative vertical velocity in the vicinity of the electrode interface. This suction is again indicative of the class of surface DBD actuators, as have been seen previously [1,55,56].

A comparison of the ionic wind produced at different operating conditions is seen in Fig. 12b by plotting the horizontal velocity profiles at x = 0, 7 and 18 mm, corresponding to dashed lines at P1, P2 and P3 in Fig. 12a. At P1, just above the electrode edge, the initial acceleration of the wall jets close to the wall is seen. This acceleration continues to P2 for all operating conditions, with the peak of the wall jet still within approximately 0.1 mm distance to the wall. The plasma at all operating conditions is active at this location (as evident by the optical emission measurements (Fig. 9). At P3, the velocity peaks are reduced and the profiles flattened, owing to viscous losses and momentum displacement within the wall jet. There is no more acceleration from the plasma at this location for all the profiles, indicating the plasma extension ending before this distance, again reconciling well with optical emissions measurements (Fig. 9). Here the plasma extension is approximately 10 mm at the operating conditions used (30 kV_{p-p} 3 kHz), while typical plasma extensions achieved from SDBDs range from 3 to 8 mm for thin dielectrics, and up to 20 mm for thicker dielectrics [1].

The plasma extension from the edge of the AC electrode increase with the increase in the applied voltage and frequency. The plasma body force increases in amplitude and imparts flow acceleration over a longer spatial extent as a function of both voltage and frequency, which is further evident as an increase in the maximum velocities seen in the wall jet, as demonstrated in Fig. 12c. The maximum velocities range from 1.33 to 3.9 m/s for the considered range in driving voltage (at constant f = 1 kHz), and from 3.1 m/s to 4.9 m/s for the considered range in frequency (at constant V_{p-p} = 30 kV). The increase from driving voltage is almost linear in trend, while the increase from frequency is leading to a stagnation in the maximum velocities. This is again in line with the behavior of SDBDs, and often attributed to the fact that an increase in frequency does not leave enough time for charge relaxation on the volume and the dielectric surface, leading to more frequent filamentary discharges. An increase in voltage however does not face this issue. [57]

Fig. 13 shows the contours of the horizontal body force distributions f_x for the respective operating conditions. For 20 kV, 1 kHz, the bulk of the body force is concentrated in a small region just downstream of the AC electrode's edge (at x = 0 mm.) With the increase in voltage and frequency the extent of the body force increases, reaching as far downstream a x = 12.5 mm, as well as reaching a height of y = 4 mm from the wall. A quantitative effect of this increase can be seen by integrating the forces in a control volume spanning from x = -6mm to 24 mm and from y = 0 to y = 11 mm. The results of this operation for all the operating conditions are seen in the plot in the inset. In addition, the

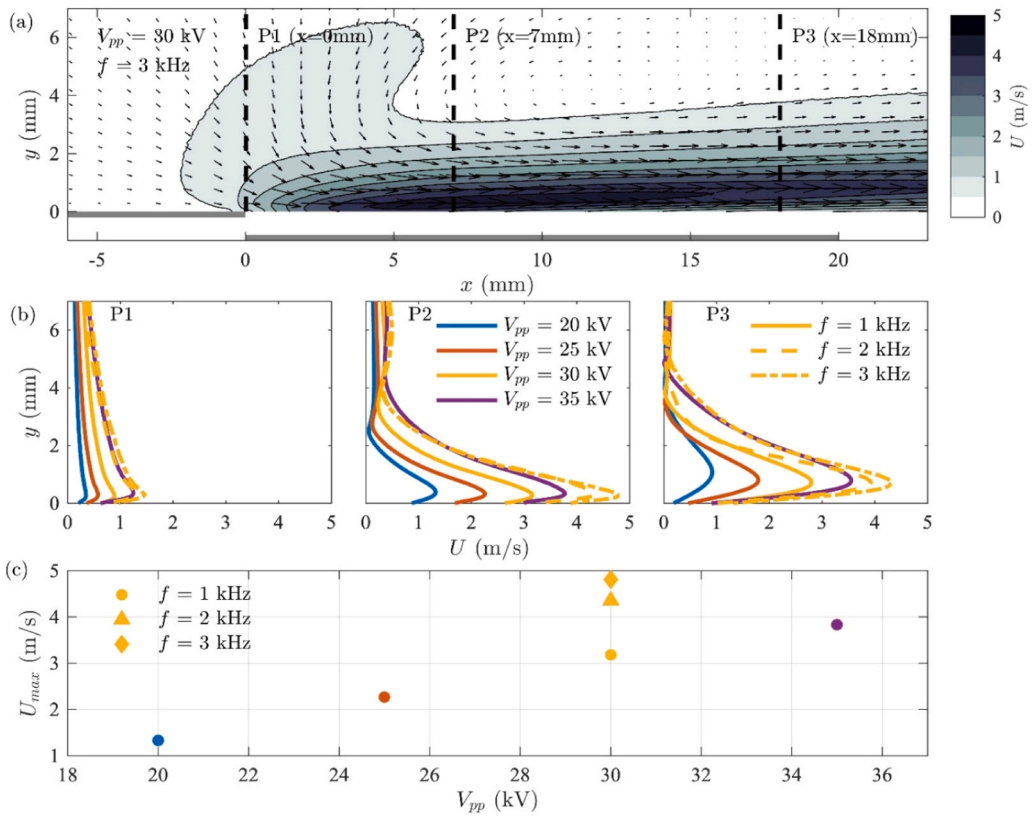

Fig. 12. a) Velocity magnitude contours of AJP-SDBD (at Vpp=30 kVp-p, f = 3 kHz) overlaid with the quiver plot of the velocity vectors. b) Horizontal velocity profiles at locations P1, P2 and P3 in a, for all the operating conditions specified in Table 3.c) Maximum induced velocity as function of Vpp and f.

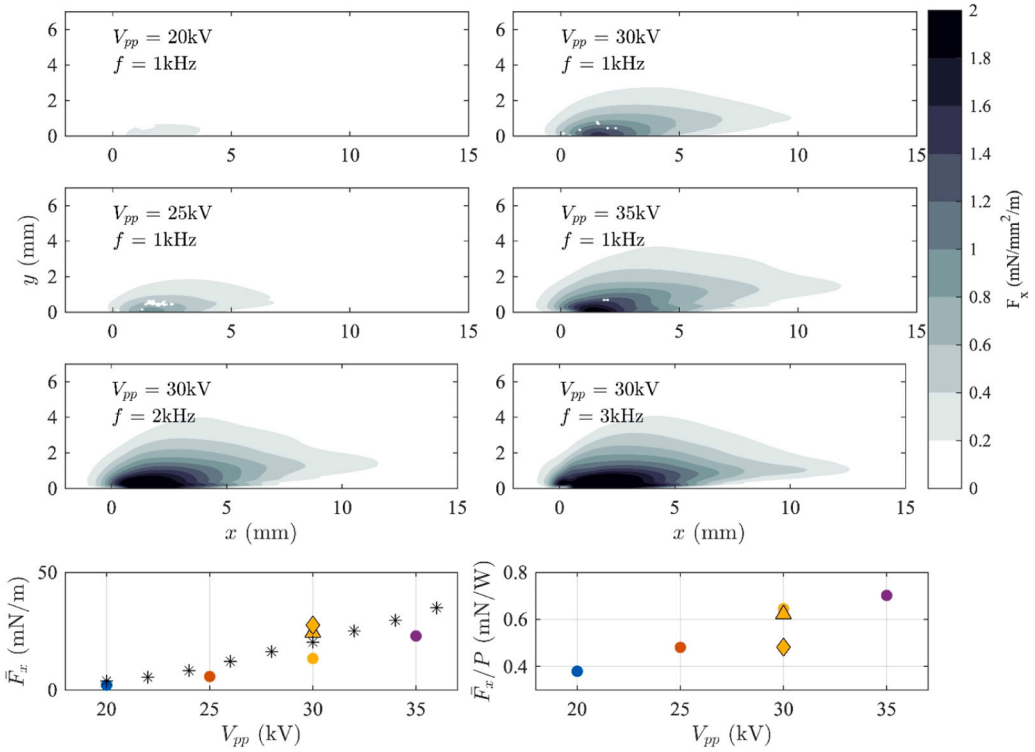

Fig. 13. Contours of the horizontal force distributions fx are shown for the operating conditions specified. White patches correspond to invalid measurement regions. Lower left plot shows the spatially integrated body force magnitudes achieved in the specified control volume vs. the voltage and frequency (for V_{pp}=30 kV, • f = 1 kHz, Δ f = 2 kHz, ◇ f = 3 kHz). Lower right plot shows normalized thrust to electrical power ratio. For comparison, reference values from a copper tape based DBD actuator of similar geometric and material properties are shown in star markers taken from the study of [58].

integrated body foce values from the present configuration are compared to a geometrically similar actuator configuration for which the electrodes were constructed using adhesive copper tape of 60 μm thickness. The copper-based actuator was tested in an integral thrust bench, using a reaction load cell as described in [58]. As evident the integrated thrust performance of the AJP-DBD is strikingly similar to the more conventional copper tape, albeit small differences can be attributed to variations in ambient conditions, power circuit and measurement methods. The comparison provides confidence that despite the extreme thinning of the active electrode enabled by the AJP method and the differences in discharge dynamics and intensity, the integral forcing performance of the actuator is not significantly affected. The body force increase with voltage follows a power curve trend typical of SDBDs, also seen in [56,59]. The increase with frequency however sees the total body force reaching an asymptote. This is in correspondence with previous works [56,59] where it is observed that increasing the frequency for a given voltage increases the body force only up to a limit, called the saturation thrust. This is again due to the effect outlined previously, where the increase in frequency beyond a certain point only increases the intensity and frequency of filamentary discharges, not allowing for the relaxation inter-pulse phases to contribute significantly to the total body force [1]. Finally, the relative efficiency of the AJP-DBD actuator is examined as the ratio of integrated force and electric input power. The values presented here are consistent with values reported for conventional copper tape based DBD actuators [56,59].

4. Discussion

The results obtained in this study clearly demonstrate the applicability of the AJP technique on the fabrication of plasma actuators. The AJP-SDBDs produced similar EHD force and presented competitive performance in terms of power consumption and thrust to power ratio when compared with conventional fabrication methods. This is attributed mainly to the micrometer thickness of the exposed electrode, which as explained in Section 3.2, can be linked to the electrostatic potential distribution and consequences on plasma regime development. These promising metrics show potential and encourage the AJP technique to be applied (and show its unique capacity) to the design of unconventional shapes with micrometer precision and features, while allowing for designs on flexible and non-planar substrates. In addition, the AJP-SDBDs showed good robustness and durability under the short-term (hours/days) stress tests, despite visually apparent electrode and dielectric degradation (see below). We attribute this to a) the enhanced adhesion properties achieved via the AJP technique and the avoidance of any adhesive layer which typically exists in conductive tapes – a potential cause of dielectric breakdown and detachment due to thermal/electrical stress and b) the ultra-smooth electrode edges (see Fig. 5) which reduce amplification of electric fields at the location of defects/sharp points - consequently reducing overintense discharges that could severely damage the electrodes/dielectric layer. These points require careful future examination to conclude on durability aspects: detailed degradation studies should be performed and focus on both the electrode edge and the dielectric material – both have shown substantial degradation in previous studies [21,60]. A preliminary inspection on the electrode edges has been performed using microscope imaging. Fig. 14 shows images of the electrode edge (top view) taken by a microscope (Nikon Eclipse MA100N) before and after several hours (see Section 3.2 for details) of plasma exposure. The images show a certain degree of degradation and the formation of “troughs” (and corresponding “crests”) with characteristic size of approx. 100 μm. These are preferential points of discharge initiation, which are clearly observed in the ICCD images. Despite this fact, the stable operation and power consumption over several hours (and days) of operation indicate that this degradation might not be critical to the AJP-SDBD operation and resulting EHD force generation.

Furthermore, we need to recognize the importance of ink adhesion in terms of durability of the proposed device. The dominant adhesion mechanisms anticipated are the Van der Waals dispersion forces and mechanical interlocking (chemical bonding less probable due to the inert character of the substrate that is not pre-activated). Moreover, it is known that thermal sintering improves cohesive strength as the solvent evaporates and the nanoparticles bind together and to the surface more uniformly, avoiding voids that can weaken adhesion. Recent studies [61] have shown though that the increase in the sintering temperature enhances neck formation in the metallic nanoparticle boundary, which boosts the connection between particles and leads to densification. Nevertheless the polymeric additive (Polyurethane binder) which is featured in the Metalon JS-A426 ink, surely plays the role of the main adhesion promoter as confirmed by the product’s technical datasheet[1] as well as similar studies which emphasized on the enhancement of the interfacial bonding between the ink and substrate [62]. However, fundamental understanding of the interplay among different adhesion mechanisms of AJP (conductive) inks on various substrates, as well as their relative contribution to adhesion strength is beyond the scope of the current work.

In addition, specific to the AJP technique, features such as sheath/carrier gas flow and high velocity jet focusing can improve anchoring of the ink to the substrate - in contrast to IJP technique. Aspects related to wettability, surface energy, roughness and other well-known parameters that affect adhesion strength, are ink and substrate specific and emphasize the need of specific and dedicated studies focusing on material/surface properties and adhesion mechanisms (including comparative adhesion durability studies) between various inks and substrates which is left for a future work. Conductive tapes typically have acrylic layers that bind to a surface when pressed (pressure sensitive adhesives) through various well known physical mechanisms (including viscoelastic dissipation). A review and analysis of these mechanisms is also outside the scope of this work.

Nevertheless, the authors recognize that reducing or eliminating degradation as well as improving adhesion strength is an essential aspect towards the establishment of AJP-SDBD actuators and thus emphasize once more on the need of detailed degradation/adhesion stress studies which should investigate different inks, different dielectric materials and their combination as well as techniques to create thin protective layers (e.g. non-reactive/resistant coatings etc.) that can withstand plasma exposure, reduce direct metal sputtering and improve durability and adhesion strength [63].

Despite the overall promising results and besides degradation, as in any other technique, AJP presents its own limitations while several aspects of its operation and handling need caution and precise control. The main limitation in terms of ink properties comes from the compatible range of dynamic viscosity (1 – 1000 cP) and particle size (if any) (up to 500 nm). In addition, the AJP principle relies (amongst others) on the laminar flow of aerosol droplets until they exit the nozzle. This implies that any visible amount of residue of material in any of the components could affect the printability of the technique. A factor that is not a limitation but mostly affects the overall printing time and can be seen as a drawback towards industrialization or mass production. We note that IJP technique face similar issues. Specific to the AJP technique is the overspray effect: The AJP aerosol mist consists of very small aerosol droplets in a stream of transport gas. The deposition is controlled by a shutter, and the splats are guided to the substrate. The small sprinkle spots located around the central splat represent small portions of atomized ink outside the main focused stream of transport gas. This affects the edge sharpness and the total tracewidth resolution. Regarding the dimensions and specifically the thickness of the dielectric material, there is no minimum height; even very thin and flexible and curved or stepped substrates could be printed on. On the contrary the deposition from 5 mm distance allows the deposition in non-planar surfaces of few

[1] https://novacentrix.com/product/js-a426-silver-nanoparticles/

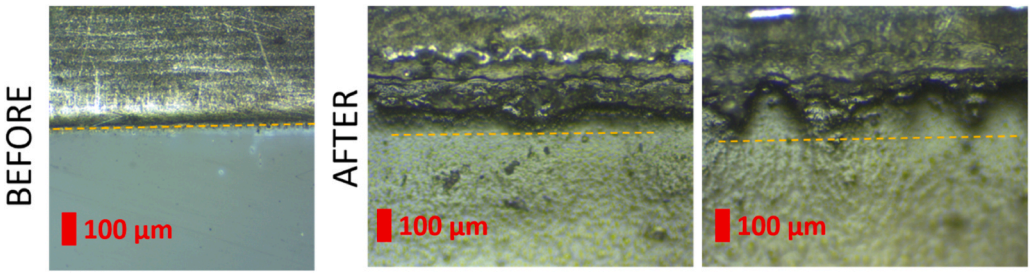

Fig. 14. Electrode degradation of the AJP-SDBD after over 30 million AC cycles of operation. "After" images show two different regions of the exposed electrode edge where different degradation patterns can be observed. The yellow dashed lines help to distinguish between the dielectric (bottom regions) and electrode (top regions) regions and they don't refer to the actual electrode outline.

mm roughness. This might be interesting for applications where the SDBD actuator needs to be applied on non-planar or curved surfaces e.g. on an airfoil or another aerodynamically critical part of an aircraft. For the specific AJP model used in this study, there is a limitation for the maximum thickness of the substrate that is 4 cm – this is due to the available area for placement of the substrate and it linked to the specific AJP model. Regarding the material of the dielectric materials there is no limitation for the AJP technique apart from the possibly poor compatibility between a specific ink and a specific substrate in terms of adhesion strength although this can be further optimized by pre-treatment techniques and/or post-treatment which includes sintering. Last, we note that the AJP technique is an open-air procedure meaning that changes in temperature/humidity affect the properties of deposition. The temperature is/can be controlled at the ink tank bath at the ultrasonic aerosolization. This is not a limitation but an important parameter that needs to be controlled.

Lastly, we note a few points on other aspects that require further investigation:

Regarding the thermal characteristics and stability of the AJP-SDBD actuators, previous works in atmospheric pressure plasma jets impinging on dielectric surfaces have shown very good agreements between OES-derived gas temperatures and plasma-induced surface temperatures measured by IR cameras and fiber optic sensors [64,65]. Besides, in the present work, the emitted light from the discharge is directly collected end-on with respect to the dielectric surface. As both streamer discharges and microdischarges burn very close to the surface (i.e. in air the streamer thickness is approximately 100 μm including a sheath of few 10 s of μm), the estimated gas temperature is a good estimation of the surface temperature in the present work. Thus, our measurements are valid for continuous operation referring to at least 30 million AC cycles. While this satisfies the scope of the present study, for accurately quantifying the long-term thermal impact, gas temperature estimation via OES (indirect method) should be ideally accompanied by direct methods for surface temperature measurements. These methods refer to IR cameras and plasma-compatible fiber optic sensors [64,65]. Nevertheless, even if these studies are combined, they cannot provide satisfactory accuracy on the discrepancies between the OES-derived gas temperature and the surface temperature at the micrometric scales of the AJP-SDBD of the present study. At the best case the spatial resolution of such diagnostics can reach few hundreds of micrometers [64,66] which is already much larger than the thickness of the electrodes.

Regarding flow measurements: in the present work, the approximate streamwise length of the body force is in the order of 10 mm (see Fig. 13), which results in an aspect ratio of 8. This is sufficiently large for edge effects to remain inconsequential to the measurements. However, the AJP method provides the opportunity for creation of complex electrode shapes, tailored to particular flow control applications. It becomes evident that electrode edge effects on the induced velocity and body force distributions need to be carefully characterized in future work. In addition, future work should also entail direct PTV measurements of a custom-built taped SDBD (same geometry/materials as AJP-SDBD) to enable side-by-side velocity/force comparison.

5. Conclusions

We have successfully demonstrated the applicability of AJP technology for the fabrication and rapid prototyping of linear SDBD actuators with ultra-fine precision. The AJP technology allows for CAD based, direct, flexible - in terms of ink and substrate selection - electrode printing with perfect alignment between asymmetrically placed electrodes. We successfully ignited the AJP-SDBDs in a wide range of operating frequencies (1 – 20 kHz) and applied voltages (12 – 40 kV_{p-p}), which operation showed quite stable plasma formation under prolonged (several hours) continuous and repetitive (several days) testing, indicating promising robustness. Compared to conventional fabrication of SDBDs using tape electrodes, the AJP-SDBDs showed higher power consumption for the same operating conditions and higher number of pulses per AC period, indicating lower breakdown/ignition voltages, higher electric fields and consequently more intense discharge under the same applied voltage. We attribute this to both the small thickness of the exposed electrode (~4 μm) and probably enhanced adhesion (e.g. due to the ink's adhesion properties owed to the polymer binder and mechanical interlocking promoted through the sintering process) and uniformity of the AJP electrodes. Advanced time-resolved imaging diagnostics, OES analysis and PTV measurement of the induced flow fields, showed that the AJP-SDBD does not alter the fundamental plasma characteristics of AC-SDBDs: a) streamer formation and elongation for several millimeters on the dielectric surface during each pulse of the positive-going cycle and microdischarge formation and space charge glow-like expansion during each pulse of the negative-going cycle. b) generation of the same types of emissive species as conventional SDBDs (mainly $N_2(C^3\Pi_u)$ and $N_2^+(B)$) c) non-thermal and non-equilibrium nature with near-ambient rotational temperature and relatively high vibrational temperature (higher during the positive-going phase) and d) EHD force and flow characteristics similar to conventional SDBDs, with maximum induced velocities in the 1–5 m/s range, maximum body force in the 1–27.5 mN/m range, both increasing with higher applied voltage and reaching saturation with increasing AC frequency.

Future work will focus on the design and characterization of non-linear AJP-SDBDs (e.g. annular where design dimensions can cause flow reversal [41]), including unconventional designs and electrode contour shapes enabled by the AJP technique. In parallel, detailed longevity and robustness studies will be performed along with an in-depth analysis of conductive inks/electrodes characteristics and possible degradation under plasma exposure. While the printed silver electrodes exhibited good adhesion and structural integrity, under plasma exposure over short time periods (hours/days) a slight electrode deformation was observed. Thus, the long-term reliability of the devices remains to be assessed via dedicated stress tests. Future work will focus on the long-term durability of AJP-SDBD under extreme conditions of voltage and frequency, while also considering more robust dielectric materials (such as alumina, quartz, etc.) demonstrating the potential of

Aerosol Jet Printing for rapid prototyping of plasma actuators that can reliably operate for long periods. Last, we aim to extend this new fabrication process of SDBDs to flexible substrates which has already shown promise in preliminary tests.

CRediT authorship contribution statement

Konstantinos Kourtzanidis: Conceptualization, Methodology, Software, Validation, Formal analysis, Investigation, Writing – Original Draft, Writing – Review & Editing, Visualization, Supervision, Project administration, Funding acquisition. **Maria Karani**: Methodology, Investigation, Visualization, Writing – Original Draft, Writing- Review & Editing. **Nicholas Vlachos**: Writing- Review & Editing. **Panagiotis Dimitrakellis**: Methodology, Investigation, Writing- Review & Editing. **Damianos Tsekourakis**: Methodology, Investigation, Visualization. **Varun Pattanshetti**: Methodology, Investigation, Formal analysis, Visualization, Writing – Original Draft, Writing- Review & Editing. **Marios Kotsonis:** Methodology, Validation, Investigation, Formal analysis, Writing – Original Draft, Writing – Review & Editing, Visualization, Supervision, Funding acquisition. **Nicolas Fagnon**: Methodology, Investigation. **Dimitrios Stefas**: Methodology, Software, Validation, Formal analysis, Investigation, Writing – Original Draft, Writing – Review & Editing, Visualization. **Kristaq Gazeli:** Methodology, Validation, Investigation, Formal analysis, Writing – Original Draft, Writing – Review & Editing, Visualization, Supervision, Funding acquisition.

Funding

The work of K. Kourtzanidis and P. Dimitrakellis was supported by the European Union Project CAIPIRINH3A, under the GA number 101191768. Views and opinions expressed are however those of the author(s) only and do not necessarily reflect those of the European Union or CINEA. Neither the European Union nor the granting authority can be held responsible for them. The work of D. Stefas and K. Gazeli was partially supported by the French Research National Agency (ANR) via the projects SPECTRON (ANR-23-CE51–0004–01), ANR ULTRAMAP (ANR-22-CE51–0027), and LabEx SEAM (ANR-10-LABX-0096 and ANR-18-IDEX-0001). The authors would like to thank Laurent Invernizzi for his assistance with the installation of optical diagnostics. M.Kotsonis was supported by the European Research Council CoG (project MetaWing, 101125132). The publication of the article in OA mode was financially supported by HEAL-Link.

Declaration of Competing Interest

The authors declare that they have no known competing financial interests or personal relationships that could have appeared to influence the work reported in this paper.

Acknowledgements

The authors would like to thank Odhisea Gazeli for providing the experimental setup rendering (Fig. 2).

Data availability

Data will be made available on request.

References

[1] N. Benard, E. Moreau, Electrical and mechanical characteristics of surface AC dielectric barrier discharge plasma actuators applied to airflow control, Exp. Fluids 55 (11) (Nov. 2014) 1846, https://doi.org/10.1007/s00348-014-1846-x.
[2] Z. Zhao, J.-M. Li, J. Zheng, Y.D. Cui, B.C. Khoo, Study of shock and induced flow dynamics by nanosecond dielectric-barrier-discharge plasma actuators, AIAA J. 53 (5) (2015) 1336–1348, https://doi.org/10.2514/1.J053420.
[3] E. Moreau, Airflow control by non-thermal plasma actuators, J. Phys. Appl. Phys. 40 (3) (Jan. 2007) 605, https://doi.org/10.1088/0022-3727/40/3/S01.
[4] T.C. Corke, C.L. Enloe, S.P. Wilkinson, Dielectric barrier discharge plasma actuators for flow control*, Annu. Rev. Fluid Mech. 42 (2010) 505–529, https://doi.org/10.1146/annurev-fluid-121108-145550.
[5] C.-C. Wang, S. Roy, Combustion stabilization using serpentine plasma actuators, Appl. Phys. Lett. 99 (4) (Jul. 2011) 041502, https://doi.org/10.1063/1.3615292.
[6] P. Audier, M. Fénot, N. Bénard, E. Moreau, Film cooling effectiveness enhancement using surface dielectric barrier discharge plasma actuator, Int. J. Heat. Fluid Flow. 62 (Dec. 2016) 247–257, https://doi.org/10.1016/j.ijheatfluidflow.2016.10.009.
[7] L.G. Lima, et al., Comparative effects of direct plasma treatment and plasma-activated media on B16F10 cancer cells using a multipoint surface dielectric barrier discharge system, J. Phys. Appl. Phys. 58 (13) (Jan. 2025) 135201, https://doi.org/10.1088/1361-6463/adac6c.
[8] S.M. Allabakshi, P.S.N.S.R. Srikar, R.K. Gangwar, S.M. Maliyekkal, Feasibility of surface dielectric barrier discharge in wastewater treatment: spectroscopic modeling, diagnostic, and dye mineralization, Sep. Purif. Technol. 296 (Sep. 2022) 121344, https://doi.org/10.1016/j.seppur.2022.121344.
[9] J. Zhang, C. Zhang, X. Xu, B. Huang, T. Shao, A review of nanosecond pulsed surface dielectric barrier discharge actuators: Effect of electrical parameters and pressures (invited paper), J. Electro 137 (Sep. 2025) 104073, https://doi.org/10.1016/j.elstat.2025.104073.
[10] Y. Bao, et al., A comprehensive study on dynamics of flames in a nanosecond pulsed discharge. Part I: Discharge formation and gas heating, Combust. Flame 275 (May 2025) 114075, https://doi.org/10.1016/j.combustflame.2025.114075.
[11] M. Nishihara, K. Takashima, J.W. Rich, I.V. Adamovich, Mach 5 bow shock control by a nanosecond pulse surface dielectric barrier discharge, Phys. Fluids 23 (6) (Jun. 2011) 066101, https://doi.org/10.1063/1.3599697.
[12] G. Neretti, P. Seri, M. Taglioli, A. Shaw, F. Iza, C.A. Borghi, Geometry optimization of linear and annular plasma synthetic jet actuators, J. Phys. Appl. Phys. 50 (1) (Nov. 2016) 015210, https://doi.org/10.1088/1361-6463/50/1/015210.
[13] F. Rodrigues, A. Mushyam, J. Pascoa, M. Trancossi, A new plasma actuator configuration for improved efficiency: the stair-shaped dielectric barrier discharge actuator, J. Phys. Appl. Phys. 52 (38) (Jul. 2019) 385201, https://doi.org/10.1088/1361-6463/ab2584.
[14] R. Hink, et al., Influence of dielectric thickness and electrode structure on the ion wind generation by micro fabricated plasma actuators, J. Phys. Appl. Phys. 53 (40) (Jul. 2020) 405201, https://doi.org/10.1088/1361-6463/ab96ea.
[15] E. Moreau, J. Cazour, N. Benard, Influence of the air-exposed active electrode shape on the electrical, optical and mechanical characteristics of a surface dielectric barrier discharge plasma actuator, J. Electro 93 (Jun. 2018) 146–153, https://doi.org/10.1016/j.elstat.2018.04.005.
[16] F.F. Rodrigues, M. Abdollahzadeh, J. Pascoa, L. Pires, Influence of exposed electrode thickness on plasma actuators performance for coupled deicing and flow control applications. Presented at the ASME 2021 Fluids Engineering Division Summer Meeting, American Society of Mechanical Engineers Digital Collection, Oct. 2021, https://doi.org/10.1115/FEDSM2021-65728.
[17] A. Debien, N. Benard, E. Moreau, Streamer inhibition for improving force and electric wind produced by DBD actuators, J. Phys. Appl. Phys. 45 (21) (May 2012) 215201, https://doi.org/10.1088/0022-3727/45/21/215201.
[18] K. Giotis, et al., Discharge dynamics in a cylindrical SDBD prototype reactor under ns-pulsed and sinusoidal AC operation, Phys. Plasmas 32 (11) (Nov. 2025) 113510, https://doi.org/10.1063/5.0284119.
[19] K. Giotis *et al.*, "Discharge dynamics in a cylindrical SDBD prototype reactor under ns-pulsed and sinusoidal AC operation," Jun. 05, 2025, arXiv: arXiv:2506.04826. doi: 10.48550/arXiv.2506.04826.
[20] R.J. Durscher, S. Roy, Three-dimensional flow measurements induced from serpentine plasma actuators in quiescent air, J. Phys. Appl. Phys. 45 (3) (Jan. 2012) 035202, https://doi.org/10.1088/0022-3727/45/3/035202.
[21] P. Warlitz, M.T. Hehner, S. Pasch, J. Serpieri, T. Blank, J. Kriegseis, On durable materials for dielectric-barrier discharge plasma actuators, Sens. Actuators Phys. 366 (Feb. 2024) 114985, https://doi.org/10.1016/j.sna.2023.114985.
[22] S. Sato, T. Enokido, K. Ashikawa, M. Matsubara, K. Kanie, N. Ohnishi, Development of a flexible dielectric-barrier-discharge plasma actuator fabricated by inkjet printing using silver nanoparticles-based ink, Sens. Actuators Phys. 330 (Oct. 2021) 112823, https://doi.org/10.1016/j.sna.2021.112823.
[23] "Experimental control of swept-wing transition through base-flow modification by plasma actuators | Journal of Fluid Mechanics | Cambridge Core." Accessed: Apr. 07, 2025. [Online]. Available: ⟨https://www.cambridge.org/core/journals/journal-of-fluid-mechanics/article/experimental-control-of-sweptwing-transition-through-baseflow-modification-by-plasma-actuators/D64F997A0E1ECC97A9F50F03927FD532#⟩.
[24] J. Kim, S. Park, W. Choe, Surface plasma with an inkjet-printed patterned electrode for low-temperature applications, Sci. Rep. 11 (1) (Jun. 2021) 12206, https://doi.org/10.1038/s41598-021-91720-3.
[25] S. Sato, et al., Fabrication and performance evaluation of full-inkjet-printed dielectric-barrier-discharge plasma actuators, Sens. Actuators Phys. 344 (Sep. 2022) 113751, https://doi.org/10.1016/j.sna.2022.113751.
[26] P. Calvert, Inkjet printing for materials and devices, Chem. Mater. 13 (10) (Oct. 2001) 3299–3305, https://doi.org/10.1021/cm0101632.
[27] T. Seifert, E. Sowade, F. Roscher, M. Wiemer, T. Gessner, R.R. Baumann, Additive manufacturing technologies compared: morphology of deposits of silver ink using inkjet and Aerosol Jet Printing, Ind. Eng. Chem. Res. 54 (2) (Jan. 2015) 769–779, https://doi.org/10.1021/ie503636c.

[28] J.D. Rurup and E.B. Secor, "Predicting Deposition Rate and Closing the Loop on Aerosol Jet Printing with In-Line Light Scattering Measurements", doi: 10.1002/adem.202201919.
[29] C. Fisher, L.N. Skolrood, K. Li, P.C. Joshi, T. Aytug, Aerosol-Jet Printed sensors for environmental, safety, and health monitoring: a review, Adv. Mater. Technol. 8 (15) (2023) 2300030, https://doi.org/10.1002/admt.202300030.
[30] G. Cummins, M.P.Y. Desmulliez, Inkjet printing of conductive materials: a review, Circuit World 38 (4) (Nov. 2012) 193–213, https://doi.org/10.1108/03056121211280413.
[31] Q. Huang, Y. Zhu, Printing conductive nanomaterials for flexible and stretchable electronics: a review of materials, processes, and applications, Adv. Mater. Technol. 4 (5) (2019) 1800546, https://doi.org/10.1002/admt.201800546.
[32] D. Ratnayake, A. Curry, C. Qu, D. Wei, E. Gerber, K. Walsh, Optimizing the conductivity of a new nanoparticle silver ink for Aerosol Jet Printing and demonstrating its use as a strain gauge, IEEE J. Flex. Electron 2 (3) (May 2023) 248–255, https://doi.org/10.1109/JFLEX.2023.3234458.
[33] M. Kotsonis, Diagnostics for characterisation of plasma actuators, Meas. Sci. Technol. 26 (9) (Aug. 2015) 092001, https://doi.org/10.1088/0957-0233/26/9/092001.
[34] J. Kriegseis, C. Schwarz, C. Tropea, S. Grundmann, Velocity-information-based force-term estimation of dielectric-barrier discharge plasma actuators, J. Phys. Appl. Phys. 46 (5) (Feb. 2013) 055202, https://doi.org/10.1088/0022-3727/46/5/055202.
[35] J.B. Wilke, "Aerodynamische Strömungssteuerung mittels dielektrischer Barriereentladungs-Plasmaaktuatoren." Accessed: Oct. 27, 2025. [Online]. Available: ⟨https://elib.dlr.de/78372/⟩.
[36] N. Benard, S. Laizet, E. Moreau, PIV-based dynamic model of EHD volume force produced by a surface dielectric barrier discharge. Proceedings of the 55th AIAA Aerospace Sciences Meeting, in AIAA SciTech Forum, American Institute of Aeronautics and Astronautics, 2017, https://doi.org/10.2514/6.2017-1579.
[37] P. Dierckx, P. Dierckx, Curve and surface fitting with splines. Monographs on Numerical Analysis, Oxford University Press, Oxford, New York, 1995.
[38] A. Sciacchitano, Uncertainty quantification in particle image velocimetry, Meas. Sci. Technol. 30 (9) (Jul. 2019) 092001, https://doi.org/10.1088/1361-6501/ab1db8.
[39] K. Kourtzanidis, G. Dufour, F. Rogier, Self-consistent modeling of a surface AC dielectric barrier discharge actuator: In-depth analysis of positive and negative phases, J. Phys. Appl. Phys. 54 (4) (Nov. 2020) 045203, https://doi.org/10.1088/1361-6463/abbcfd.
[40] A. Debien, N. Benard, E. Moreau, Streamer inhibition for improving force and electric wind produced by DBD actuators, J. Phys. Appl. Phys. 45 (21) (May 2012) 215201, https://doi.org/10.1088/0022-3727/45/21/215201.
[41] H. Borradaile, K. Kourtzanidis, F. Rogier, K.-S. Choi, X. Mao, Flow reversal in millimetric annular DBD plasma actuator, J. Phys. Appl. Phys. 54 (34) (Jun. 2021) 345202, https://doi.org/10.1088/1361-6463/ac0145.
[42] K. Mitsuhashi, A. Komuro, K. Suzuki, C. Natsume, A. Ando, Spatiotemporal variations of the electrical potential on surface dielectric barrier discharges, Plasma Sources Sci. Technol. 30 (4) (Apr. 2021) 04LT02, https://doi.org/10.1088/1361-6595/abefa7.
[43] Y. Lagmich, T. Callegari, L.C. Pitchford, J.P. Boeuf, Model description of surface dielectric barrier discharges for flow control, J. Phys. Appl. Phys. 41 (9) (Apr. 2008) 095205, https://doi.org/10.1088/0022-3727/41/9/095205.
[44] S. Sato, N. Ohnishi, Role of surface discharge dynamics in the generation of electrohydrodynamic force: toward performance improvement of dielectric barrier discharge plasma actuators, J. Phys. Appl. Phys. 58 (14) (Feb. 2025) 143002, https://doi.org/10.1088/1361-6463/adb3af.
[45] K. Kourtzanidis, G. Dufour, F. Rogier, The electrohydrodynamic force distribution in surface AC dielectric barrier discharge actuators: do streamers dictate the ionic wind profiles? J. Phys. Appl. Phys. 54 (26) (Apr. 2021) 26LT01, https://doi.org/10.1088/1361-6463/abf53e.
[46] G.P. Vafakos, P.K. Papadopoulos, P. Svarnas, A three-stage plasma model based on one-way coupling of plasma dynamics, ionic motion, and fluid flow: application to DBD plasma actuators, J. Appl. Phys. 137 (4) (Jan. 2025) 043302, https://doi.org/10.1063/5.0242676.
[47] D. Stefas, et al., Machine learning assisted optical diagnostics on a cylindrical surface dielectric barrier discharge, J. Phys. Appl. Phys. 57 (45) (Nov. 2024) 455206, https://doi.org/10.1088/1361-6463/ad6ba1.
[48] K. Giotis, P. Svarnas, E. Amanatides, K. Gazeli, G. Lombardi, P.K. Papadopoulos, Ionization wave propagation and cathode sheath formation due to surface dielectric-barrier discharge sustained in pulsed mode, Plasma Sci. Technol. 25 (11) (Nov. 2023) 115402, https://doi.org/10.1088/2058-6272/acdb52.
[49] J. Voráč, L. Kusýn, P. Synek, Deducing rotational quantum-state distributions from overlapping molecular spectra, Rev. Sci. Instrum. 90 (12) (Dec. 2019) 123102, https://doi.org/10.1063/1.5128455.
[50] J. Voráč, P. Synek, L. Potočňáková, J. Hnilica, V. Kudrle, Batch processing of overlapping molecular spectra as a tool for spatio-temporal diagnostics of power modulated microwave plasma jet, Plasma Sources Sci. Technol. 26 (2) (Jan. 2017) 025010, https://doi.org/10.1088/1361-6595/aa51f0.
[51] J. Voráč, P. Synek, V. Procházka, T. Hoder, State-by-state emission spectra fitting for non-equilibrium plasmas: OH spectra of surface barrier discharge at argon/water interface, J. Phys. Appl. Phys. 50 (29) (Jul. 2017) 294002, https://doi.org/10.1088/1361-6463/aa7570.
[52] T.D. Nguyen, N. Sadeghi, Rotational and vibrational distributions of N2(C 3Πu) excited by state-selected Ar(3P2) and Ar(3P0) metastable atoms, Chem. Phys. 79 (1) (Aug. 1983) 41–55, https://doi.org/10.1016/0301-0104(83)85137-4.
[53] K. Gazeli, et al., Physical interpretation of a pulsed atmospheric pressure plasma jet following parametric study of the UV–to–NIR emission, Phys. Plasmas 27 (12) (Dec. 2020) 123503, https://doi.org/10.1063/5.0031065.
[54] S. Nijdam, J. Teunissen, U. Ebert, The physics of streamer discharge phenomena, Plasma Sources Sci. Technol. 29 (10) (Nov. 2020) 103001, https://doi.org/10.1088/1361-6595/abaa05.
[55] J.P. Murphy, J. Kriegseis, P. Lavoie, Scaling of maximum velocity, body force, and power consumption of dielectric barrier discharge plasma actuators via particle image velocimetry, J. Appl. Phys. 113 (24) (Jun. 2013) 243301, https://doi.org/10.1063/1.4811225.
[56] M. Kotsonis, L. Veldhuis, S. Ghaemi, R. Giepman, Experimental study on the body force field of dielectric barrier discharge actuators. Proceedings of the 41st Plasmadynamics and Lasers Conference, in Fluid Dynamics and Co-located Conferences, American Institute of Aeronautics and Astronautics, 2010, https://doi.org/10.2514/6.2010-4630.
[57] M. Forte, J. Jolibois, J. Pons, E. Moreau, G. Touchard, M. Cazalens, Optimization of a dielectric barrier discharge actuator by stationary and non-stationary measurements of the induced flow velocity: application to airflow control, Exp. Fluids 43 (6) (Nov. 2007) 917–928, https://doi.org/10.1007/s00348-007-0362-7.
[58] M. Kotsonis, S. Ghaemi, Performance improvement of plasma actuators using asymmetric high voltage waveforms, J. Phys. Appl. Phys. 45 (4) (Jan. 2012) 045204, https://doi.org/10.1088/0022-3727/45/4/045204.
[59] F.O. Thomas, T.C. Corke, M. Iqbal, A. Kozlov, D. Schatzman, Optimization of dielectric barrier discharge plasma actuators for active aerodynamic flow control, AIAA J. 47 (9) (Sep. 2009) 2169–2178, https://doi.org/10.2514/1.41588.
[60] R.E. Hanson, N.M. Houser, P. Lavoie, Dielectric material degradation monitoring of dielectric barrier discharge plasma actuators, J. Appl. Phys. 115 (4) (Jan. 2014) 043301, https://doi.org/10.1063/1.4862309.
[61] H.-J. Park, K. Ryu, H.-L. Lee, Y.-J. Moon, J.Y. Hwang, S.J. Moon, Physical characteristics of sintered silver nanoparticle inks with different sizes during furnace sintering, Materials 17 (5) (Jan. 2024) 978, https://doi.org/10.3390/ma17050978.
[62] Y. Niu, et al., Aerosol Jet Printing of synthesized Ag/Ag nanowires hybrid inks for highly sensitive, wide-range conformal temperature sensing, Adv. Mater. Technol. 11 (4) (2026) e01654, https://doi.org/10.1002/admt.202501654.
[63] R. Elsersawy, A. Rahman, C. Sakib-Uz-Zaman, M.A.H. Khondoker, Multifunctional inks in aerosol jet printing: performance, challenges, and applications, Front. Manuf. Technol. 5 (May 2025), https://doi.org/10.3389/fmtec.2025.1558209.
[64] K. Shumikhin, et al., Investigating the effects of atomic oxygen cold plasma surface cleaning on the oil paint, Adv. Mater. Interfaces 12 (22) (2025) e00220, https://doi.org/10.1002/admi.202500220.
[65] K. Gazeli, et al., Experimental investigation of a ns-pulsed argon plasma jet for the fast desorption of weakly volatile organic compounds deposited on glass substrates at variable electric potential, J. Phys. Appl. Phys. 53 (47) (Sep. 2020) 475202, https://doi.org/10.1088/1361-6463/aba870.
[66] A. Brisset, et al., Experimental study of the effect of water vapor on dynamics of a high electric field non-equilibrium diffuse discharge in air, J. Phys. Appl. Phys. 54 (21) (Mar. 2021) 215204, https://doi.org/10.1088/1361-6463/abe81e.

Konstantinos Kourtzanidis received a Ph.D. in plasma engineering and fluid dynamics from ISAE-SUPAERO, France in 2014. He is a collaborating researcher at the Advanced Renewable Technologies for Energy & Materials Integrated Systems (ARTEMIS) Laboratory of the Chemical Process & Energy Resources Institute (CPERI) at Centre for Research & Technology Hellas (CERTH), Thessaloniki, Greece. He has also worked as a researcher at ONERA – The French Aerospace Lab (Toulouse, France) and the University of Texas at Austin (Austin, USA). His current research interests focus on plasma actuators, plasma assisted combustion, compressible flows and multiphysics modeling and simulations of low-temperature plasmas.

Maria Karani works at CERTH (Centre for Research & Technology Hellas) as scientific personnel and currently focusing on thin film deposition methods using the Aerosol Jet Printing technology. In 2011 she obtained her Bachelor in Physics from the Aristotle University of Thessaloniki (AUTH), then in 2015 acquired a MSc in Nanotechnology from Chalmers Technical University in Gothenburg, Sweden. Her career path includes consulting services for Volvo Trucks AB as a Simulation Engineer for Hybrid/Full Electric Heavy Duty vehicles and working as a Research Engineer at SiTEk Electro Optics AB producing and developing silicon based optoelectronic devices.

Nickolas Vlachos has been a collaborating researcher at the Centre for Research and Technology Hellas (CERTH) in Thessaloniki, Greece, working in publicly funded research projects as well as in applied research for industry contract projects for over 23 years. He holds a Ph.D. in computational aerodynamics (1999) from the Dept. of Aeronautical Engineering, University of Bristol, UK. His research is focused on aerosol technology, porous materials and associated chemical reactors, Li-ion batteries and advanced computational methods supporting the aforementioned topics.

Panagiotis Dimitrakellis received a Ph.D. from the Department of Chemical Engineering, University of Patras, Greece in 2014. He is currently a collaborating researcher at Centre for Research and Technology Hellas (CERTH) in Thessaloniki, Greece. His research is focused on non-thermal plasma processing for advanced materials fabrication and green chemical synthesis.

Damianos Tsekourakis is a student at The School of Chemical Engineering of the Aristotle University of Thessaloniki, currently completing his integrated master degree. He is

employed at Centre for Research and Technology Hellas (CERTH) in Thessaloniki, Greece where he supports the aerosol jet printing activities relevant to plasma actuators.

Nikolaos Hastas received his Ph.D. from Aristotle University of Thessaloniki, School of Physics, in 2005. His current research interests focus on transport properties of condensed matter.

Varun Pattanshetti received his M.S. degree in Aerospace Engineering from TU Delft, The Netherlands, with a specialisation in Aerodynamics.

Marios Kotsonis received a Ph.D. from Delft University of Technology, The Netherlands in 2012. He is currently Professor of Flow Control at the same university. His interests cover fundamental flow physics of transitional flows and the development and application of flow control methods. He is a holder of ERC Starting and Consolidator grants and NWO Veni and Vici awards.

Dimitrios Stefas is a Postdoctoral Researcher at the Laboratoire des Sciences des Procédés et des Matériaux (LSPM), CNRS, France. He obtained his Ph.D. in Physics in 2023 from the University of Patras, Greece. His research interests focus on advanced optical diagnostics applied to a wide range of non-equilibrium plasmas, extending from low-pressure plasmas to atmospheric pressure discharges and laser-produced plasmas. He employs Machine Learning to bridge diagnostics with fundamental plasma understanding and applications, ranging from in-situ monitoring of PECVD processes to material classification based on laser-produced plasmas.

Nicolas Fagnon is a R&D Engineer at CNRS, at the Laboratory of Process and Materials Sciences, CNRS, France since 2001, after holding positions as a technician and then assistant engineer in instrumentation and experimental techniques. Specialized in metrology, measurement and control systems, signal processing, and LabVIEW development (CLAD certification). Proficient in CAD using SolidWorks, conventional machining, and vacuum, high-pressure, and plasma technologies.

Kristaq Gazeli is a Research Scientist at the LSPM laboratory, jointly affiliated with CNRS and Université Sorbonne Paris Nord (USPN). He has been Postdoctoral Researcher at the LPGP (CNRS, Université Paris-Saclay, France) and the LSPM laboratories, Invited Researcher at the University of Cyprus (UCY) and at USPN, and Marie Skłodowska-Curie Fellow at UCY. He holds a joint PhD in Physics and Electrical and Computer Engineering from UPPA (France) and the University of Patras (Greece). His research focuses on physics of non-thermal plasmas, plasma–surface interactions, and development of advanced optical diagnostics (fast and ultrafast imaging, emission spectroscopy, LIF/TALIF, etc.).